

**Improving Measurements of the Mixing State and Mass
Concentration of Particulate Emissions from Aircraft Engines**

Matthew Alexander Dickau

A thesis submitted in partial fulfillment of the requirements for the degree of

Master of Science

Department of Mechanical Engineering

University of Alberta

© Matthew Alexander Dickau, 2016

Abstract

This research is focused towards improving techniques used to measure particulate emissions from aircraft engines, on two fronts: first, to characterize and quantify the mixing state of particulate emissions; and second, to calibrate black carbon mass instruments with a traceable mass concentration measurement system. Mixing state refers to the relative proportions of volatile and non-volatile material in an aerosol, and the way these components are combined. The mixing state affects optical and moisture absorption properties, and quantifying it is therefore important for studying an aerosol's climate impact. Described in this work is a method to quantify the mixing state by measuring the mass distributions of different components of an aerosol. The method is demonstrated with a test aerosol and then used to measure the mixing state of soot from a Gnome aircraft engine.

Instruments that can measure the mass concentration of black carbon in real time are being increasingly used in research and industry, but these instruments (the Laser Induced Incandescence 300 and the Micro Soot Sensor) use indirect techniques, measuring parameters other than the actual mass of particulate, and therefore require calibration. Previously, it has been shown that a centrifugal particle mass analyzer (CPMA) can be used in conjunction with an aerosol electrometer to traceably generate an aerosol with known mass concentration. This system can be used to rapidly calibrate particle mass instruments (on the order of minutes), without the time-consuming process of filter sampling which is often used for calibration and prone to sampling artifacts. Here the feasibility of the CPMA-electrometer system as a calibration method is demonstrated, using two LII 300 instruments and two MSS instruments.

Preface

A version of Chapter 2 of this thesis has been submitted for publication as:

Dickau, M., Olfert, J., Stettler, M., Boies, A., Momenimovahed, A., Thomson, K., Smallwood, G., Johnson, M. (2016) Methodology for Quantifying the Mixing State of an Aerosol. *Aerosol Science and Technology*, 50.

It is currently in the process of revisions. J. Olfert, M. Stettler, A. Momenimovahed, K. Thomson, and G. Smallwood assisted me with the experiment, and M. Johnson hosted the experiment at Rolls-Royce. M. Stettler contributed to the introduction. All authors contributed to the editorial process.

Everyone who contributed to the experimental and editorial work on Chapter 2 also contributed in the same capacity to Chapter 3, a version of which is being prepared for submission for publication in *Atmospheric Environment*. I was the primary author on both Chapter 2 and 3.

A version of Chapter 4 of this thesis has been published as:

Dickau, M., Johnson, T., Thomson, K., Smallwood, G., Olfert, J. (2015) Demonstration of the CPMA-Electrometer System for Calibrating Black Carbon Particulate Mass Instruments, *Aerosol Science and Technology*, 49(3), 152-158.

T. Johnson, K. Thomson, and J. Olfert assisted me with the experimental work, and G. Smallwood hosted at the National Research Council of Canada. I was again the primary author on this chapter, and all authors contributed to the editorial process.

The Introduction and Conclusion of this thesis are my original work.

Acknowledgements

Funding for this research was provided by the Transport Canada Clean Transportation Program, the National Sciences and Engineering Research Council (NSERC), and Alberta Innovates Technology Futures (AITF). Marc Johnson at Rolls-Royce hosted the experiments for Chapters 2 and 3, and Adam Boies at Catalytic Instruments provided the denuders for the experiments. Greg Smallwood at the National Research Council of Canada hosted the experiment for Chapter 4, and Dan Clavel assisted us in the setup. MDS Aero Support Corporation also supported the setup of that experiment by lending us aid in the form of Tyler Johnson.

I want to personally thank my supervisor, Jason Olfert, for his incredible support, advice, and assistance in making this happen, as well as the members of my family for being there for me over the years, always with steadfast encouragement. Last but certainly not least, I want to thank my wife, Lillian. Thank you for your love, support, and patience with me while I finished this thesis!

Table of Contents

1. Introduction	1
1.1 Impact of Particulate Emissions	1
1.2 Particulate Emissions from Aircraft Engines	1
1.3 Mixing State	4
1.4 Regulation of Particulate Emissions in Aviation	5
1.5 Overview of Research.....	6
1.6 Bibliography	6
2. Methodology for Quantifying the Mixing State of an Aerosol.....	10
2.1 Introduction	10
2.1.1 Overview of Instrumentation	10
2.1.2 Previous Techniques for Characterizing Mixing State	12
2.2 Method.....	14
2.2.1 Experimental Setup	16
2.2.2 Size Distribution Measurement.....	16
2.2.3 Volatile Particle Number Fraction	16
2.2.4 Volatile Mass Fraction	20
2.2.5 Mixing State Mass Distributions.....	24
2.3 Results and Discussion.....	26
2.3.1 Volatile Mass Fraction	26
2.3.2 Size Dependence of Particle Mass	26
2.3.3 Externally Mixed Volatile Particle Fraction	27
2.3.4 Mixing State Size and Mass Distributions.....	28
2.4 Conclusion	31
2.5 Bibliography	32

3. Mixing State of Particles Emitted from a Gas Turbine Engine	36
3.1 Experimental Setup.....	36
3.2 Results	39
3.2.1 Effective Density	39
3.2.2 Volatile Mass Fraction	42
3.2.3 Volatile Particle Number Fraction	43
3.2.4 Size and Mass Distributions.....	43
3.3 Conclusion	46
3.4 Bibliography	47
4. Demonstration of the CPMA-Electrometer System for Calibrating Black Carbon Particulate Mass Instruments	50
4.1 Introduction	50
4.2 Theory.....	52
4.3 Experimental Setup.....	54
4.4 Results and Discussion.....	57
4.4.1 Linearity and Uncertainty	57
4.4.2 Effect of Charge Neutralizer.....	60
4.4.3 Effect of CPMA Resolution	61
4.5 Conclusions	62
4.6 Bibliography	62
5. Conclusion	64
5.1 Summary and Conclusions	64
5.2 Future Work	65
Complete Bibliography	67

Appendix A. Supplementary Material to Mixing State of Particles Emitted from a Gas Turbine Engine	74
A.1 Volatile Number and Mass Fractions with Upstream Catalytic Stripper	74

List of Figures

Figure 1.1 Typical components of particulate matter emissions from aircraft engines	2
Figure 2.1 DMA schematic. Small particles (high mobility) are dragged too quickly by the sheath flow and miss the exit port; large particles (low mobility) are not dragged quickly enough and do not reach the port.	11
Figure 2.2 CPMA/APM schematic. Particles with higher mass are flung outwards by the centrifugal force; less massive particles are pulled inwards by the electrostatic force.	11
Figure 2.3 Experimental setup for measurements of a) size distribution, b) volatile particle fraction, and c) volatile mass fraction.	15
Figure 2.4 Ratio of penetration efficiencies of the hot catalytic denuder over the cold denuder, versus particle mobility diameter.....	19
Figure 2.5 Mass distributions (distribution of particle concentration over mass) of size selected soot from the high OC setting, showing how the distribution changes when denuded at DMA set points of 38 nm, 100 nm, and 225 nm (left to right).	21
Figure 2.6 Volatile mass fraction versus undenuded particle mobility diameter.	27
Figure 2.7 Median mass of the undenuded particles versus particle mobility diameter.	27
Figure 2.8 Externally mixed volatile particle number fraction versus undenuded particle mobility diameter.....	28
Figure 2.9 Size distributions of the soot from a) high EC and b) high OC showing the number concentration of each component of the sample versus particle mobility diameter.	29

Figure 2.10 Mixing state of the soot from a) high EC and b) high OC. Mass distribution showing the mass concentration of each component of the sample versus particle mobility diameter.....	29
Figure 3.1 Experimental setup for measurements of the volatile mass fraction and volatile particle number fraction, showing the sampling system and the DMA-CPMA setup.	37
Figure 3.2 Effective density versus particle mobility diameter for particles from a Gnome engine at 22,000 RPM and 13,000 RPM, with and without a denuder placed upstream of the DMA.	40
Figure 3.3 Comparison of the effective densities of denuded Gnome engine particulate to that of a CFM56-5B4/2P turbine (Johnson et al. 2013).....	41
Figure 3.4 Comparison of the effective densities of undenuded Gnome engine particulate to that of a CFM56-5B4/2P turbine (Lobo et al. 2015) and a CFM56-7B26/3 (Abegglen et al. 2015, Durdina et al. 2014).	41
Figure 3.5 Volatile mass fraction versus particle mobility diameter for particulate from a Gnome engine at 22,000 RPM and 13,000 RPM.....	42
Figure 3.6 Volatile particle number fraction particle mobility diameter for particulate from a Gnome engine at 22,000 RPM and 13,000 RPM.....	43
Figure 3.7 Number distributions of Gnome engine particulate from a) the 13,000 RPM condition and b) the 22,000 RPM condition, showing the number concentration of each component (volatile and non-volatile) at different particle mobility diameters..	45
Figure 3.8 Mass distributions of Gnome engine particulate from a) the 13,000 RPM condition and b) the 22,000 RPM condition, showing the mass concentration of each component (non-volatile, internally mixed volatile, and externally mixed volatile) at different particle mobility diameters.....	45
Figure 4.1 Diagram of experimental setup.	54

Figure 4.2 Comparison of soot mass concentration measurements by the CPMA-electrometer system to those by (a) two LII 300 instruments and (b) two MSS instruments, all measurements with a neutralizer and with the CPMA set at resolution of approximately $R_{CPMA} = 6.5$ 57

Figure 4.3 Mass concentration measurements with and without a neutralizer for (a) the LII 300 SN0343 and (b) the MSS SN1187, all measurements with the CPMA set at resolution of approximately $R_{CPMA} = 6.5$ 60

Figure 4.4 Mass concentration measurements with the CPMA set at resolutions of approximately $R_{CPMA} = 4.5$ and $R_{CPMA} = 6.5$ for (a) the LII 300 SN0343 and (b) the MSS SN1187, both with a neutralizer. 60

Figure A.1 Volatile mass fraction versus particle mobility diameter for particulate from a Gnome engine at 22,000 RPM and 13,000 RPM, with the upstream catalytic stripper (CS) either off or on. 74

Figure A.2 Volatile particle number fraction versus particle mobility diameter for particulate from a Gnome engine at 22,000 RPM and 13,000 RPM, with the upstream catalytic stripper (CS) either off or on..... 74

List of Tables

Table 2.1 Flow rates of the miniCAST High EC and High OC set points..... 16

Table 2.2 Mass fractions of the different material components of the soot from the different set points..... 30

Table 3.1 Total mass fractions for the different components of the particulate at different engine conditions. 46

List of Variables

C	Prefactor for effective density power law
$\frac{dN}{d \ln d_m}$	Number distribution over size (also called size distribution)
$\frac{dN_{nv}}{d \ln d_m}$	Non-volatile particle number distribution
$\frac{dN_v}{d \ln d_m}$	Volatile particle number distribution
$\frac{dN}{d \ln m_p}$	Number distribution over mass (also called mass distribution)
d_m	Mobility-equivalent particle diameter
$\frac{dM}{d \ln d_m}$	Mass distribution
$\frac{dM_{ext}}{d \ln d_m}$	Externally mixed volatile mass distribution
$\frac{dM_{int}}{d \ln d_m}$	Internally mixed volatile mass distribution
$\frac{dM_{nv}}{d \ln d_m}$	Non-volatile mass distribution
$\epsilon_{D,pen}$	Penetration efficiency of denuded line
$\epsilon_{U,pen}$	Penetration efficiency of undenuded line
f_{vm}	Volatile mass fraction
f_{vp}	Volatile particle number fraction
I	Current
M_0	Uncharged mass concentration
$M_{classified}$	Mass concentration classified by CPMA
m_D	Mass of denuded particle
M_{NIOSH}	Mass concentration measured by NIOSH 5040 method
m_p or m	Particle mass
m_U	Mass of undenuded particle

m_{vol}	Mass of purely volatile particle
N_{+i}	Number concentration of particles with i charges
n	Exponent for effective density power law
$n_{\text{D,actual}}$	Actual denuded particle concentration
$n_{\text{D,measured}}$	Measured denuded particle concentration
$n_{\text{D,t}}$	Measured denuded concentration of the test aerosol
$n_{\text{D,s}}$	Measured denuded concentration of the sample aerosol
$n_{\text{U,actual}}$	Actual undenuded particle concentration
$n_{\text{U,measured}}$	Measured undenuded particle concentration
$n_{\text{U,t}}$	Measured undenuded concentration of the test aerosol
$n_{\text{U,s}}$	Measured undenuded concentration of the sample aerosol
$n_i t$	Product of ion concentration and residence time
ω	CPMA angular velocity
Q	Volume flow rate
q	Particle charge
r_1	CPMA inner radius
r_2	CPMA outer radius
R^2	Coefficient of determination in linear regression
r_c	CPMA mean radius
R_{CPMA}	CPMA resolution
Re	Reynolds number
r_{pen}	Ratio of penetration efficiencies
RSD_{NIOSH}	Relative standard deviation of NIOSH 5040 method
ρ_{eff}	Effective density

ρ_{vol}	Density of volatile material
s	Particle mass-to-charge ratio
σ_{NIOSH}	Standard deviation of NIOSH 5040 method
V	CPMA voltage

List of Acronyms

AMS	Aerosol mass spectrometer
APM	Aerosol particle mass analyzer
BC	Black carbon
CD	Catalytic denuder
CPC	Condensation particle counter
CPMA	Centrifugal particle mass analyzer
CS	Catalytic stripper
DMA	Differential mobility analyzer
EC	Elemental carbon
FID	Flame ionization detector
HEPA	High efficiency particulate arrestance
LII	Laser-induced incandescence
LS	Light scattering
MAC	Mass absorption cross-section
MSS	Micro-Soot Sensor
OC	Organic carbon
rBC	Refractory black carbon
RPM	Rotations per minute
SP2	Single particle soot photometer
SP-AMS	Soot particle aerosol mass spectrometer
SEM	Scanning electron microscopy
TDMA	Tandem differential mobility analyzer

1. Introduction

Aerosols, solid or liquid particles suspended in a gas, are an important factor in our environment. Clouds (water droplets in the atmosphere), smoke (soot particles in combustion gases), and dust (various debris in air) are examples of the ubiquity of aerosols around us. Aerosols and the particulates that comprise them are an active area of research, and an especially important aspect of aerosol research is the study of the particulates that human activity produces. We must understand them to understand how we are impacting the environment, and what impact that has on us in return.

1.1 Impact of Particulate Emissions

Combustion, especially of fossil fuels, is a significant source of anthropogenic particulate emissions. Particulate matter from combustion degrades local air quality by causing smog (Unal et al., 2005, Woody et al., 2011), and adversely affects human health (Lighty et al., 2000, Pope, 2000). In particular, particulate matter increases rates of respiratory and cardiovascular disease (Burnett et al., 2014), because small particles can easily be inhaled into the lungs and even transfer from the lungs into the bloodstream. There they can cause irritation, inflammation, and other detrimental effects to respiratory and cardiovascular tissues. Furthermore, soot emissions in the atmosphere impact global climate by absorbing radiation (Bond et al., 2013, Myhre et al., 2013) and influencing cloud formation, properties, and lifetime (Boucher et al., 2013). These effects can cause a net heating or cooling effect on Earth's climate depending on the chemical composition of the particulates (Lee et al., 2010).

1.2 Particulate Emissions from Aircraft Engines

The aviation sector is a major contributor to particulate emissions from combustion, and aviation emissions are only increasing. Commercial air traffic is expected to more than double its 2010 levels by the year 2030 (ICAO, 2013). Particulate emissions from aircraft have been shown to affect health and the environment not only near airports (Yim et al., 2013), but also on a hemispheric scale (Barrett et al., 2010). The energy density requirements for heavier-than-air transportation necessitate that aircraft will be

burning fossil fuels for many years to come; therefore, being able to study and measure particulate emissions from aircraft engines is of great importance.

Particulates from aircraft engines are generally composed of non-volatile carbonaceous material, thought to be mostly solid carbon, and often mixed with semi-volatile or volatile material, thought to be mostly liquid hydrocarbons. Both of these kinds of materials arise from incomplete combustion of hydrocarbon fuels and may also contain other trace compounds (e.g. sulfuric acid). Assuming carbonaceous composition, the non-volatile material may be variously referred to as elemental carbon (EC), black carbon (BC), or refractory black carbon (rBC) depending on the technique used to measure it (Petzold et al., 2013); while the volatile material may be referred to as organic carbon (OC). However, there may be other kinds of chemical compounds present in these materials.

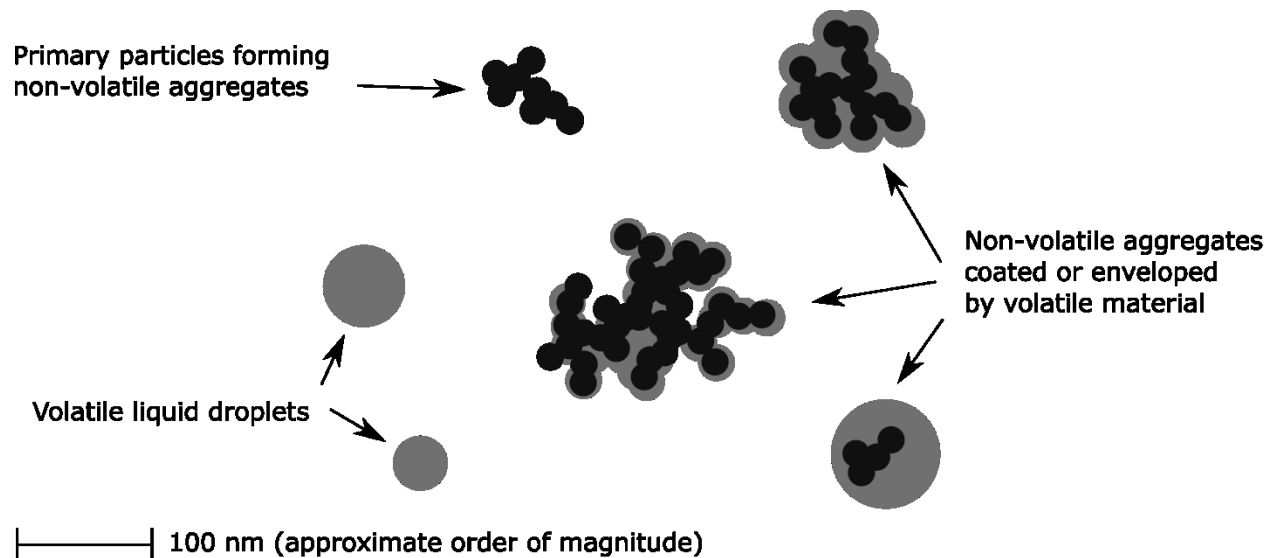


Figure 1.1: Typical components of particulate matter emissions from aircraft engines.

The solid elemental carbon forms into roughly spherical primary particles, typically smaller than approximately 40 nm in diameter (Boies et al., 2015). These primary particles coagulate to form larger aggregate soot particles with fractal-like branching chain structures. Because of their complex structure, the physical size of such soot particles is not well defined, so the mobility-equivalent diameter is generally used to characterize the particle size instead. The mobility of a particle is its drift velocity

through a fluid divided by the drag force it experiences due to that motion. This is a constant for a given particle and fluid in low Reynolds number flows ($Re \ll 1$). The mobility-equivalent diameter is the diameter of a sphere with the same mobility as the particle. These aggregate soot particles generally occur in distributions with median mobility-equivalent diameters from 10 nm to 70 nm (Boies et al., 2015, Lobo et al., 2015).

Unlike size, the mass of an aggregate soot particle is well defined. To compare different groups of particles, or to compare particles to other materials, the mass and the mobility diameter are often used to calculate the effective density, which is the mass divided by the volume of the mobility-equivalent sphere. Effective densities of soot particles are typically found to follow an approximate power-law relationship with mobility equivalent diameter:

$$\rho_{\text{eff}} = C d_m^{-n} \quad (1.1)$$

where ρ_{eff} is the effective density, d_m is the mobility-equivalent diameter, and C and n are parameters. This can indicate the degree of branching or packing of the primary particles in the aggregates; the more the effective density decreases with increasing size, the less tightly packed the primary particles. Effective densities are generally in the range of 400 kg/m^3 at a mobility diameter of 200 nm, to 1200 kg/m^3 at a mobility diameter of 25 nm (Johnson et al., 2015, Lobo et al., 2015, Durdina et al., 2014, Abegglen et al., 2015).

Often, volatile organic carbon is mixed with the non-volatile component of soot. This material may either form independent particles separate from the black carbon aggregates, known as external mixing, or it may condense onto the black carbon to fill voids, form a coating, or entirely envelop the particles, situations known as internal mixing (Bond et al., 2013). Further condensation, adsorption, and coagulation can lead to internal mixing after the aerosol has formed (Cappa et al., 2012, Zhang et al., 2008). The way that the volatile material mixes with the non-volatile material is characterized by the mixing state.

1.3 Mixing State

In an aerosol population comprised of both volatile and non-volatile material (or more generally, any two different kinds of material), the different materials may be mixed together in different ways. External mixing is when the different materials form different particles, and we refer to a particle comprised solely of volatile material or solely of non-volatile material as externally mixed. Internal mixing is when both materials are present in the same particle, and we refer to a particle comprised of both volatile and non-volatile material as internally mixed. The mixing state of the population is the proportions of the volatile and non-volatile material present in each state, comprising an internally or externally mixed particle.

The mixing state of soot particulates is important in determining its properties. Optical characteristics of black carbon particles have been shown to be significantly affected by the mixing state. Laboratory studies have demonstrated enhancements of the mass absorption cross-section (MAC) for internally mixed BC particles with large OC mass fractions (Bond et al. 2013, Cross et al., 2010). Atmospheric aerosol studies show that MAC enhancement of internally mixed BC particles may vary significantly with the proportion of non-BC material (Chan et al., 2011) and the particle structure (Cappa et al., 2012). Optical properties determine the radiation absorption of particles, and therefore are important both for studying the climate impact of particulate emissions, and for particle measurement.

The mixing state also affects the moisture absorption properties of black carbon particles and therefore the interactions between particles and clouds. More hygroscopic (moisture-absorbing) particles will serve as nucleation sites for cloud droplets at lower humidities than will less hygroscopic particles (McFiggans et al., 2006). The mixing state, and the composition and relative mass of the volatile material, has been shown to affect the hygroscopic properties of atmospheric BC particles (Liu et al., 2013, Kuwata et al., 2009). As providing nucleation sites for cloud formation is the principle way that particulates interact with clouds, knowing these properties is also necessary for studying their climate impact. For both optical properties and cloud condensation nuclei activity,

knowledge of the mixing state provides important context for understanding how those properties arise.

1.4 Regulation of Particulate Emissions in Aviation

Aircraft emissions are currently regulated during take-off and landing using the smoke number, an optical technique that measures the optical reflectivity of particulate collected on a filter (ICAO, 2008, SAE, 2011). The smoke number regulation ensures that exhaust plumes from aircraft engines do not visibly emit particles, but the measurement is not directly correlated to the mass or number of particles emitted, though some correlations have been made (Stettler et al., 2013). Since light scattering is proportional to the diameter squared, it is biased towards larger particles and may not detect smaller particles, which are still dangerous to human health.

Because the effects of particulate emissions on health and climate are size dependent, properly quantifying emissions requires measurement of both number concentration and mass concentration. SAE has begun developing standards and recommended practices to regulate emissions in this way, which has led to the development of SAE AIR6241 (SAE, 2013). This draft standard proposes that aircraft particulate emissions be regulated based on the non-volatile particle number and mass concentration. Methods for the measurement of non-volatile particle number concentration are well known. SAE E-31 (Aircraft Exhaust Emissions Measurement Committee) is investigating methods for the measurement of the non-volatile mass concentration. The instruments under consideration are the laser-induced incandescence instrument (LII 300) and the photoacoustic Micro-Soot Sensor (MSS). These instruments can measure non-volatile black carbon mass concentration in real time; however, they require calibration by a traceable mass concentration measurement system. To more fully understand the particulate emissions of aircraft engines, these non-volatile measurements would have to be coupled with a way to measure the mixing state, allowing one to account for the volatile material.

1.5 Overview of Research

This research addresses the need to i) characterize and quantify the mixing state of particulate emissions from aircraft engines, and ii) calibrate mass instruments with a traceable mass concentration measurement system, both towards the purpose of advancing our ability to measure and understand these sources of particulate emissions. In Chapter 2, a methodology for measuring the mixing state of an aerosol is described and demonstrated. In Chapter 3, the mixing state of a typical aircraft gas turbine engine is measured. In Chapter 4, the CPMA-electrometer system is demonstrated as a suitable calibration method for mass concentration measurement instruments. Finally, Chapter 5 closes this research with an overall discussion and summary of its conclusions.

1.6 Bibliography

- Abegglen, M., Durdina, L., Brem, B., Wang, J., Rindlisbacher, T., Corbin, J., et. al. (2015). Effective density and mass–mobility exponents of particulate matter in aircraft turbine exhaust: Dependence on engine thrust and particle size. *Journal of Aerosol Science*, 88, 135-147.
- Barrett, Steven R. H., Britter, Rex E., Waitz, Ian A. (2010). Global Mortality Attributable to Aircraft Cruise Emissions, *Environmental Science and Technology*. 44 (19):7736–7742.
- Boies, A., Stettler, M., Swanson, J., Johnson, T., Olfert, J., Johnson, M., ... Rogak, S. (2015). Particle Emissions Characteristics of a Gas Turbine with a Double Annular Combustor. *Aerosol Science and Technology*, 49(9), 842-855. doi: 10.1080/02786826.2015.1078452
- Bond, T. C., Doherty, S. J., Fahey, D. W., Forster, P. M., Berntsen, T., DeAngelo, B. J., ... Zender, C. S. (2013). Bounding the role of black carbon in the climate system: A scientific assessment. *Journal of Geophysical Research: Atmospheres*, 118(11), 5380–5552. <http://doi.org/10.1002/jgrd.50171>
- Burnett, R. T., Pope, C. Arden, I., Ezzati, M., Olives, C., Lim, S. S., Mehta, S., ... Cohen, A. (2014). An Integrated Risk Function for Estimating the Global Burden of Disease Attributable to Ambient Fine Particulate Matter Exposure. *Environmental Health Perspectives*.
- Boucher, O., Randall, D., Artaxo, P., Bretherton, C., Feingold, G., & Forster, P., et al (2013). Clouds and aerosols. In T. F. Stocker, D. Qin, G.-K. Plattner, M. Tignor, S. K. Allen, J. Boschung, A. Nauels, Y. Xia, V. Bex, & P. M. Midgley (Eds.), *Climate Change 2013: The physical science basis. Contribution of Working Group I to the Fifth Assessment Report*

of the Intergovernmental Panel on Climate Change. *Cambridge University Press*: Cambridge, UK; New York, NY, USA

- Cappa, C. D., Onasch, T. B., Massoli, P., Worsnop, D. R., Bates, T. S., Cross, E. S., ... Zaveri, R. A. (2012). Radiative absorption enhancements due to the mixing state of atmospheric black carbon. *Science* (New York, N.Y.), 337(6098), 1078–81. <http://doi.org/10.1126/science.1223447>
- Chan, T. W., Brook, J. R., Smallwood, G. J., & Lu, G. (2011). Time-resolved measurements of black carbon light absorption enhancement in urban and near-urban locations of southern Ontario, Canada. *Atmospheric Chemistry and Physics*, 11(20), 10407–10432. <http://doi.org/10.5194/acp-11-10407-2011>
- Cross, E. S., Onasch, T. B., Ahern, A., Wrobel, W., Slowik, J. G., Olfert, J., ... Davidovits, P. (2010). Soot Particle Studies—Instrument Inter-Comparison—Project Overview. *Aerosol Science and Technology*, 44(8), 592–611. Retrieved from <http://dx.doi.org/10.1080/02786826.2010.482113>
- Durdina, L., Brem, B.T., Abegglen, M., Lobo, P., Rindlisbacher, T., & Thomson, K.A., et al. (2014). Determination of PM mass emissions from an aircraft turbine engine using particle effective density. *Atmospheric Environment*, 99, 500–507, <http://dx.doi.org/10.1016/j.atmosenv.2014.10.018>
- ICAO. (2008). ICAO Annex 16: Environmental Protection, Volume II – Aircraft Engine Emissions. *International Civil Aviation Organization*, Montreal, Canada.
- ICAO. (2013). International Civil Aviation Organization. (2013) ICAO 2013 Environmental Report. *International Civil Aviation Organization*, Montreal, Canada. Accessed online at http://cfapp.icao.int/Environmental-Report-2013/files/assets/common/downloads/ICAO_2013_Environmental_Report.pdf
- Johnson, T., Olfert, J., Symonds, J., Johnson, M., Rindlisbacher, T., Swanson, J., et al. (2015). Effective density and mass-mobility exponent of aircraft turbine particulate matter. *Journal of Propulsion and Power*, 31(2), 573-581.
- Kuwata, M., Kondo, Y., & Takegawa, N. (2009). Critical condensed mass for activation of black carbon as cloud condensation nuclei in Tokyo. *Journal of Geophysical Research*, 114(D20), D20202. <http://doi.org/10.1029/2009JD012086>
- Lee, D. S., Pitari, G., Grewe, V., Gierens, K., Penner, J. E., Petzold, A., Prather, M. J., Schaumann, U., Bais, A., Berntsen, T., Iachetti, D., Lim, L. L., Sausen, R. (2010). Transport impacts on atmosphere and climate: Aviation. *Atmospheric Environment*. 44(37):4678-4734.
- Lighty, J. S., Veranth, J. M., & Sarofim, A. F. (2000). Combustion aerosols: Factors governing their size and composition and implications to human health. *Journal of the Air & Waste*

Management Association, 50(9), 1565–1618,
<http://dx.doi.org/10.1080/10473289.2000.10464197>.

- Liu, D., Allan, J., Whitehead, J., Young, D., Flynn, M., Coe, H., ... Bandy, B. (2013). Ambient black carbon particle hygroscopic properties controlled by mixing state and composition. *Atmospheric Chemistry and Physics*, 13(4), 2015–2029. <http://doi.org/10.5194/acp-13-2015-2013>
- Lobo, P., Durdina, L., Smallwood, G., Rindlisbacher, T., Siegerist, F., Black, E., et al. (2015). Measurement of Aircraft Engine Non-Volatile PM Emissions: Results of the Aviation-Particle Regulatory Instrumentation Demonstration Experiment (A-PRIDE) 4 Campaign. *Aerosol Science and Technology*, 49(7), 472-484.
- McFiggans, G., Artaxo, P., Baltensperger, U., Coe, H., Facchini, M. C., Feingold, G., ... Weingartner, E. (2006). The effect of physical and chemical aerosol properties on warm cloud droplet activation. *Atmospheric Chemistry and Physics*, 6(9), 2593–2649. <http://doi.org/10.5194/acp-6-2593-2006>
- Myhre, G., Shindell, D., Breon, F.-M., Collins, W., Fuglestedt, J., Huang, J., ... Zhang, H. (2013). *Anthropogenic and Natural Radiative Forcing*. In T. F. Stocker, D. Qin, G.-K. Plattner, M. Tignor, S. K. Allen, J. Boschung, ... P. M. Midgley (Eds.), *Climate Change 2013: The Physical Science Basis. Contribution of Working Group I to the Fifth Assessment Report of the Intergovernmental Panel on Climate Change*. Cambridge, UK and New York, NY, USA: *Cambridge University Press*. Retrieved from http://www.climatechange2013.org/images/report/WG1AR5_Chapter08_FINAL.pdf
- Petzold, A., Ogren, J., Fiebig, M., Laj, P., Li, S.-M., Baltensperger, U., ... Zhang, X.-Y. (2013). Recommendations for reporting "black carbon" measurements. *Atmospheric Chemistry and Physics*, 13, 8365-8379. doi:10.5194/acp-13-8365-2013
- Pope, C. A. (2000). What do epidemiologic findings tell us about health effects of environmental aerosols? *Journal of Aerosol Med.* 13(4):335-354.
- SAE. (2011). SAE Aerospace Recommended Practice 1179 Rev D, "Aircraft gas turbine engine exhaust smoke measurement". *Society of Automotive Engineers International*.
- SAE. (2013). SAE Aerospace Information Report 6241, "Procedure for the continuous sampling and measurement of non-volatile particle emissions from aircraft turbine engines". *Society of Automotive Engineers International*.
- Stettler, Marc E. J., Swanson, Jacob J., Barrett, Steven R. H., Bois, Adam M. (2013) Updated Correlation Between Aircraft Smoke Number and Black Carbon Concentration. *Aerosol Science and Technology*. 47(11):1205-1214.
- Unal, A., Hu, Y. T., Chang, M. E., Odman, M. T., and Russell, A. G., "Airport Related Emissions and Impacts on Air Quality: Application to the Atlanta International Airport," *Atmospheric*

Environment, Vol. 39, No. 32, 2005, pp. 5787–5798.
doi:10.1016/j.atmosenv.2005.05.051

Woody, M., Baek, B. H., Adelman, Z., Omary, M., Lam, Y. F., West, J. J., and Arunachalam, S., “An Assessment of Aviation’s Contribution to Current and Future Fine Particulate Matter in the United States,” *Atmospheric Environment*, Vol. 45, No. 20, 2011, pp. 3424–3433.
doi:10.1016/j.atmosenv.2011.03.041

Yim, Steve H. L., Stettler, Marc E. J., Barrett, Steven R. H. (2013). Air quality and public health impacts of UK airports. Part II: Impacts and policy assessment. *Atmospheric Environment*. 67:184-192.

Zhang, R., Khalizov, A. F., Pagels, J., Zhang, D., Xue, H., & McMurry, P. H. (2008). Variability in morphology, hygroscopicity, and optical properties of soot aerosols during atmospheric processing. *Proceedings of the National Academy of Sciences of the United States of America*, 105(30), 10291–6. Retrieved from <http://www.pnas.org/cgi/content/abstract/105/30/10291>

2. Methodology for Quantifying the Mixing State of an Aerosol¹

2.1 Introduction

The mixing state of particulate emissions from aircraft engines has a significant influence on its optical properties and its interaction with the environment, so it is important to be able to measure the mixing state quantitatively. This chapter demonstrates a methodology for simultaneously quantifying the mixing state of an aerosol, producing a mass distribution (i.e. $dM/d\log d_m$) separated into non-volatile, internally mixed volatile, and externally mixed volatile components. The non-volatile material could be further resolved into internally and externally mixed components; but in the data presented the non-volatile material is observed to be either all externally mixed or all internally mixed. Volatile material is operationally defined as material removed by a catalytic denuder heated to 350°C. This temperature was selected in accordance with the Particle Measurement Programme for automotive particulate emissions who define non-volatile particulate as particles remaining after heating to 300 to 400 °C with sufficient residence time to evaporate, and prevent the re-nucleation of, 30 nm tetracontane particles (UNECE Regulation No. 83). A similar operational definition is proposed for future aircraft certification (SAE 2013). Under this definition the majority of OC substances produced in incomplete combustion of hydrocarbons are volatile, as are some inorganic materials (e.g. sulfuric acid, water); while elemental carbon or BC materials are non-volatile. It is assumed that the volatile material does not undergo pyrolysis that transforms it into non-volatile material.

2.1.1 Overview of Instrumentation

The described methodology characterizes the mixing state using a differential mobility analyzer (DMA; Knutson & Whitby, 1975), a centrifugal particle mass analyzer (CPMA; Olfert & Collings, 2005), a catalytic denuder (often called a catalytic stripper; Swanson & Schulz, 2013) and a condensation particle counter (CPC). The catalytic denuder passes the aerosol flow through a heated metal catalyst to evaporate volatile material and

¹ A version of this chapter has been submitted for publication as Dickau, M., Olfert, J., Stettler, M., Boies, A., Momenimovahed, A., Thomson, K., Smallwood, G., Johnson, M. (2016) Methodology for Quantifying the Mixing State of an Aerosol. *Aerosol Science and Technology*, 50.

either catalytically oxidize it, forming products with high saturation vapour pressures (e.g. CO_2 , H_2O) that do not condense at the temperature and pressure of the aerosol, or it simply may have low enough partial pressure to prevent recondensing on the particles. This removes the volatile material. The CPC counts particles by causing supersaturated butanol vapour to condense onto the particles, making them big enough to be detected optically, by obstructing a laser beam. The DMA and CPMA (as well as the aerosol particle mass analyzer, or APM; Ehara et al., 1996) are particle classifiers, meaning they take an aerosol sample in, and then only allow certain particles to pass out again, removing the rest from the flow. A classifier for a certain property allows only those particles within a specific narrow range of that property to pass through, where the range can be adjusted based on the classifier settings.

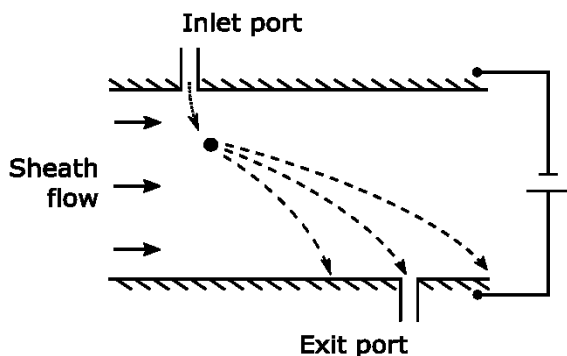


Figure 2.1: DMA schematic. Small particles (high mobility) are dragged too quickly by the sheath flow and miss the exit port; large particles (low mobility) are not dragged quickly enough and do not reach the port.

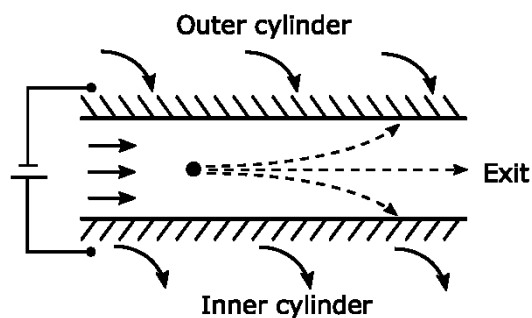


Figure 2.2: CPMA/APM schematic. Particles with higher mass are flung outwards by the centrifugal force; less massive particles are pulled inwards by the electrostatic force.

The DMA, shown in Figure 2.1, classifies particles by electrical mobility, which is the product of mobility and the charge carried by the particle. It does this by balancing electrostatic and drag forces on the particles inside of a column with a sheath flow. The sheath flow drags the particles along the column, while the electrostatic force pulls the particles from one side of the column to the other. Only particles within a narrow range of electrical mobilities reach the other side at the exit port and are able to exit the DMA. Prior to entering the DMA, the particles are usually passed through a neutralizer that places a known charge distribution on the particles. In this state the majority of charged particles have only a single elementary charge (either positive or negative, but only one

sign of charge can escape the DMA), and so the electrical mobility can be considered equivalent to the mobility. In this way, the DMA can be said to classify by mobility, or mobility-equivalent diameter (provided one corrects for the few multiply charged particles that may be present).

Similarly, the CPMA and APM, shown in Figure 2.2, both classify particles by mass-to-charge ratio. They do this by balancing electrostatic and centrifugal forces on the particles as they flow in a narrow gap between two concentric rotating cylinders. The flow is entrained to rotate with the cylinders, subjecting the particles to a centrifugal force outwards. A potential difference between the cylinders creates an electrostatic force pulling the particles inwards. Only particles within a narrow range of mass-to-charge ratios escape from the end of the classifier. The CPMA differs from the APM by rotating the two cylinders at slightly different speeds, which has the effect of focusing the desired particles to the center of the gap to reduce losses. If the particles are charged with a neutralizer (as is commonly done with the DMA, see above) the mass-to-charge ratio can often be considered equivalent to the mass, since the majority of particles have the same charge.

2.1.2 Previous Techniques for Characterizing Mixing State²

Several techniques are available to determine the mixing state of BC-containing particles, these can be differentiated into population averaged and single particle techniques. Single particle mixing state techniques include scanning electron microscopy, refractory BC³ (rBC) incandescence, and particle mass spectrometry. Single particle measurements using these techniques are typically aggregated to give population-level characteristics. Scanning electron microscopy techniques have been used to visually classify the mixing state and quantify morphological characteristics of ambient soot particles (China et al., 2015; China et al., 2013), however these techniques are unable to quantify the mass ratios of BC to non-BC components. The single particle soot photometer (SP2) instrument has been developed to quantify rBC

² Marc Stettler (Cambridge University Engineering Department) contributed to the content of this section as part of our submission to Aerosol Science and Technology.

³ Refractory black carbon is used to refer to measurements derived from incandescence methods. (Petzold et al., 2013)

using single particle incandescence signals (Stephens et al., 2003). The incandescence signal provides information as to whether an individual particle contains rBC and time difference between incandescence and light scattering signals has been used to classify the mixing state of particles as ‘thinly coated’ or ‘thickly coated’ (McMeeking et al., 2011; Moteki & Kondo, 2007). However, the lower detection limit of the SP2 is approximately 0.3 fg (Q. Wang et al., 2014; J.P. Schwarz et al., 2010), which is approximately 70 nm in diameter for a volume equivalent sphere or approximately 100 nm in diameter for a mobility equivalent sphere from a typical engine combustion source⁴, whereas the count median mobility diameter for many combustion sources (diesel engines, gasoline direct injection engines, gas turbine engines) are below 100 nm. The aerosol mass spectrometer (AMS) was designed to enable quantification and speciation of non-refractory aerosol components (Jayne et al., 2000). Recent developments and incorporation of the SP2 principle into the AMS have enabled quantification of rBC in addition to non-refractory aerosol components on population-averaged basis in an instrument called the soot particle aerosol mass spectrometer (SP-AMS) (Cross et al., 2010; Onasch et al., 2012). The addition of a light-scattering module (LS-SP-AMS) allows for the rBC and non-refractory aerosols on a single-particle basis. Recent application of the LS-SP-AMS to urban aerosols by Lee et al. (2015) indicates that measurements of the mixing state of BC-containing particles are currently constrained by a detection limit of around 25 fg of rBC per particle (far larger than the median particle mass for most rBC sources) and that rBC-containing particle number and mass measurements may be underestimated.

Of the aerosol population techniques, tandem differential mobility analyzer⁵ methods involve classifying an aerosol sample with a first DMA, coating or denuding the resultant monodisperse aerosol to add or remove volatile material respectively, followed by a second DMA such that the change in mobility diameter, d_m , and mobility-based particle volume can be quantified (Petzold et al., 2005). However, this technique is dependent on the particle morphology and for non-spherical particles large amounts of coating can

⁴ Graves (2015) shows the soot from several diesel, gasoline direct injection, gasoline port-injection, and natural gas direct injection compression-ignition engines follow a mass mobility relationship of $m = 0.0686 (\text{kg m}^{-2.49}) d_m^{2.49}$, where d_m is the mobility equivalent diameter of the particle.

⁵ See Section 2.1.1 for a description of how a differential mobility analyzer (DMA) works.

be added without a detectable change in the mobility diameter. For example, Ghazi and Olfert (2013) showed that the mass of a soot particle could be increased up to 3 times with a coating of dioctyl sebacate without a measurable increase in the mobility diameter. Furthermore, this technique may be susceptible to changes in the structure and mobility of the BC aggregates during coating or denuding (Pagels et al., 2009). Thus, the quantification of the amount of volatile material coated on a non-spherical particle is prone to large errors. A derivative of this method is to use a DMA in tandem with a particle mass analyzer (either an aerosol particle mass analyzer or centrifugal particle mass analyzer).⁶ In this technique, a DMA is used to select a monodisperse aerosol that is then denuded or coated, followed by a particle mass analyzer so that the change in particle mass statistics with and without denuding/coating of the aerosol can be quantified. This technique has been used to determine the mass fraction of volatile material on coated particles from flames (Zhang et al., 2008; Ghazi & Olfert, 2013; Ghazi, Tjong, et al. 2013; Pagels et al., 2009; Schnitzler et al., 2014), gasoline direct injection engines (Momenimovahed and Olfert, 2015), natural-gas direct-injection compression-ignition engine (Graves et al., 2015), and ambient aerosol (Kuwata et al. (2009), Rissler et al., 2014). Sakurai et al. (2003) combined a tandem DMA setup to measure particle volatility via mobility diameter change with a DMA-APM to measure volatility via mass change, in order to measure volatility at different particle sizes.

2.2 Method

This method builds upon DMA-mass analyzer techniques described in section 2.1.2 to quantify the mobility diameter dependent mixing state of an aerosol and explicitly includes the externally mixed volatile particle number and mass fractions. While similar techniques have been used before (Sakurai et al. 2003), the method described here uses a simpler system to better characterize particle losses, allowing greater accuracy in the volatile number fraction measurements. In this study, a CPMA has been used to quantify particle mass, but the methods described could also be implemented with an APM. The method is demonstrated on particles generated by a diffusion flame.

⁶ See Section 2.1.1 for a description of how an aerosol particle mass analyzer (APM) or a centrifugal particle mass analyzer (CPMA) functions.

The methodology quantifies the mixing state using with three independent measurements. First, the sample is measured using a DMA and CPC or scanning mobility particle sizer (SMPS; Wang & Flagan, 1990) to determine the count mobility size distribution by data inversion (Stolzenburg & McMurry, 2008) as shown in Figure 2.3a. Second, the volatile number fraction of the particles at each mobility size is determined, measuring the number of externally mixed particles that are purely volatile using a DMA, catalytic denuder, and CPC as shown in Figure 2.3b. Third, the volatile mass fraction of the internally mixed particles at each size is found, measuring the proportion of the mass that is volatile using a DMA, catalytic denuder, CPMA, and CPC as shown in Figure 2.3c. From these measurements, the mass distribution is calculated.

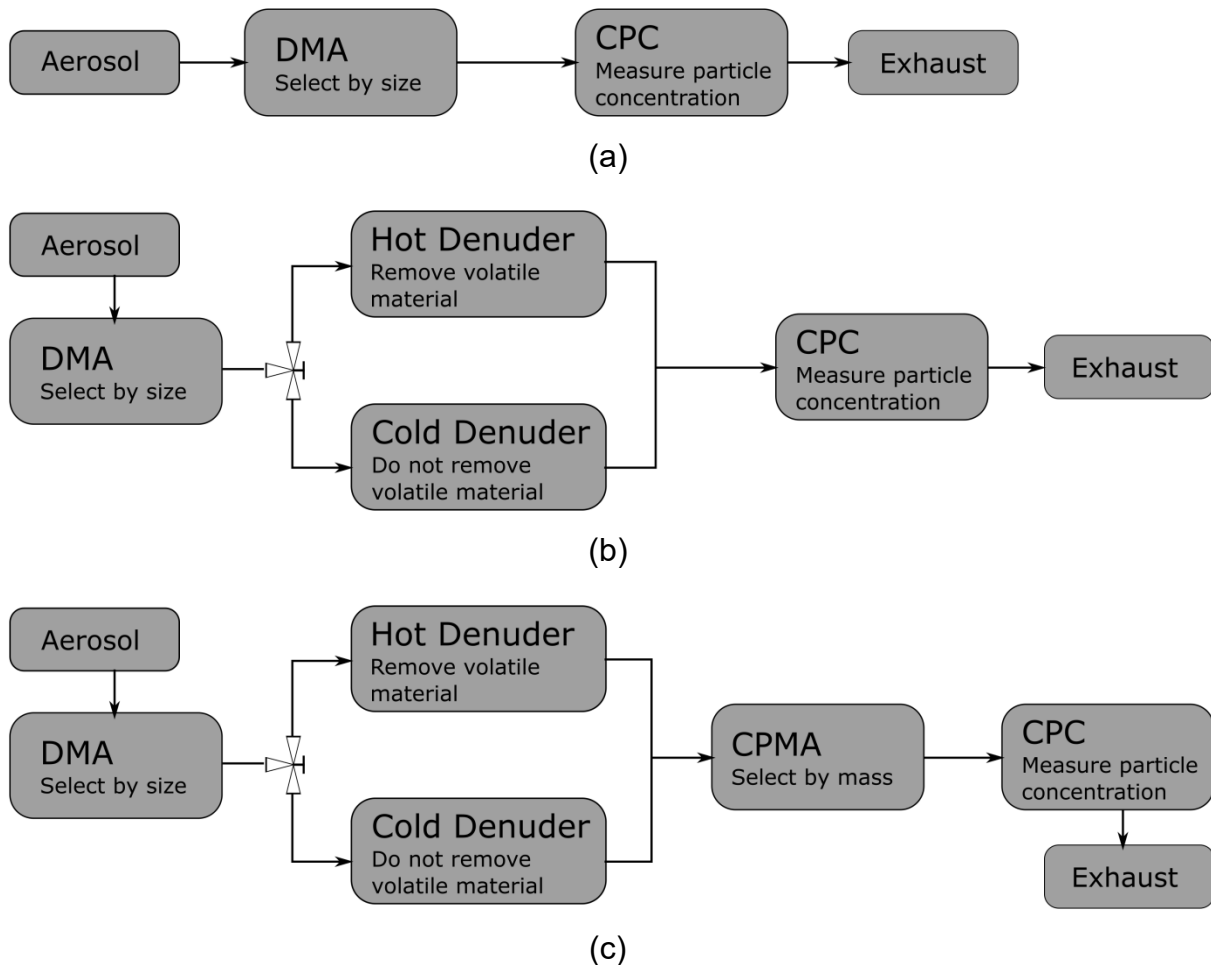


Figure 2.3: Experimental setup for measurements of a) size distribution, b) volatile particle fraction, and c) volatile mass fraction.

2.2.1 Experimental Setup

The methodology is demonstrated with measurements on particles produced by a miniCAST soot generator (model 5201C, Jing Ltd) using two different settings. The “High EC” setting is a high elemental carbon (EC) set point with very little volatile material. Conversely, the “High OC” setting is a high organic carbon (OC) set point with a substantial amount of volatile material. Table 2.1 shows the flow rate settings for these set points.

Table 2.1: Flow rates of the miniCAST High EC and High OC set points.

Flame Condition	High EC	High OC
C ₃ H ₈	60 mL/min	60 mL/min
Mixing N ₂	0 mL/min	0 mL/min
Oxidation Air	1.55 L/min	1.2 L/min
Dilution Air	20 L/min	20 L/min
Quench N ₂	7 L/min	7 L/min
Global Equivalence Ratio	0.92	1.19

2.2.2 Size Distribution Measurement

The size distributions of the samples were measured using a DMA (Model 3081, TSI Inc.) and a CPC (Model 3776, TSI Inc.) as shown in Figure 2.3a. For the size distribution measurement of the high EC setting, a sheath flow of 3 L/min and aerosol flow of 0.3 L/min was used. A sheath flow of 15 L/min and aerosol flow of 1.5 L/min was used for the high OC size distribution measurement, and for the other measurements in this study. The aerosol was classified by electrical mobility in the DMA, which scans through a range of electrical mobility while counting the particles with the CPC to measure their number concentration. The size distribution is calculated from this data using the inversion routine in the TSI AIM software (version 9).

2.2.3 Volatile Particle Number Fraction

Figure 2.3b shows the experimental setup for measuring the volatile particle number fraction. The aerosol sample was first size-selected using the DMA that selects the particles of a given range of electrical mobility equivalent diameters. Next, the sample was sent either through a heated catalytic denuder at 350 °C (Model CS015; Catalytic Instruments), or through a denuder at ambient temperature of the same model. The hot catalytic denuder removed the volatile material from the sample (denuded), while the

cold denuder left it unaffected (undenuded). The catalytic denuder has an average gas residence time of 1.1 s at 350 °C and 0.5 s at 20 °C for flow rates of 1.5 standard L/min. By our operational definition of volatility, the volatile material was precisely the material removed by the denuder at 350 °C and flowrate of 1.5 standard L/min. If other denuder temperatures or flow rates were used the amount of volatile material that would evaporate could differ. The particles were then counted in the CPC to measure the number concentration. The difference between the denuded and undenuded concentrations is the number concentration of externally mixed volatile particles removed by the denuder. The lower detection of the CPC used in this study was 2.5 nm, therefore, denuded particles with a diameter less than 2.5 nm would be counted as an externally mixed volatile particle. Switching back and forth between the denuded and undenuded lines allowed repeated measurements so as to average out random fluctuations. Repeating this procedure and classifying the sample at different mobility diameters generated the volatile particle number fraction across the size range of the sample.

The measurement of number concentration is sensitive to particle losses, and in particular the ratio between the denuded and undenuded concentrations is sensitive to the ratio of the penetration efficiencies of the hot catalytic denuder and the cold denuder. To minimize this difference, the two lines were made to be the same length and incorporated the same model of denuder, with the cold denuder simply remaining inactive (i.e. unheated). The ratio of penetration efficiencies was measured in order to account for particle deposition due to thermophoresis and diffusion as follows.

2.2.3.1 Measurement of Penetration Ratio

Given that the measured number concentration is equal to the actual concentration times the penetration efficiency of the denuder system, the relationship between the actual concentration ratio and the measured concentration ratio is;

$$\frac{n_{D,actual}}{n_{U,actual}} = \frac{n_{D,measured}}{r_{pen} n_{U,measured}}, \quad (2.1)$$

where,

$$r_{\text{pen}} = \frac{\epsilon_{\text{D,pen}}}{\epsilon_{\text{U,pen}}}, \quad (2.2)$$

where n_{D} and n_{U} are the denuded and undenuded number concentrations, actual or measured; $\epsilon_{\text{D,pen}}$ and $\epsilon_{\text{U,pen}}$ are the penetration efficiencies of the hot and cold denuders, respectively; and r_{pen} is the ratio of these penetration efficiencies. In the case of purely non-volatile test aerosols, the actual number concentration should be unaffected by denuding, so that the ratio of the penetration efficiencies of the denuded and undenuded lines is equal to the ratio of the measured number concentrations of the test aerosol. In general these are functions of particle size. Therefore,

$$r_{\text{pen}}(d_{\text{m}}) = \frac{n_{\text{D,t}}(d_{\text{m}})}{n_{\text{U,t}}(d_{\text{m}})} \quad (2.3)$$

where d_{m} is the particle mobility diameter, and $n_{\text{D,t}}$ and $n_{\text{U,t}}$ are the measured number concentrations of the denuded and undenuded non-volatile test aerosols.

The penetration ratio was measured using two different test aerosols: an atomized salt (NaCl) aerosol and a high EC soot, chosen to be purely non-volatile. The NaCl aerosol was generated using an atomizer (Model 3076, TSI Inc.) with a diffusion dryer. The high EC soot was generated with a miniCAST (Model 4202, Jing Ltd) operating at the following flow rates: 50 mL/min C_3H_8 , 1.5 L/min oxidation air, 5.5 L/min quench N_2 , and 30 L/min dilution air.⁷ This soot was denuded upstream of the experiment at 350 °C with a third catalytic denuder identical to the ones used in rest of the setup (CS015; Catalytic Instruments). Again, by definition, all particles leaving the upstream catalytic denuder are non-volatile. After particle generation and conditioning, the penetration ratio measurements used the same experimental setup and method as the volatile particle fraction measurements shown in Figure 2.3b.

⁷ A different miniCAST burner was used for these measurements as the one used in the main part of the experiment was unavailable.

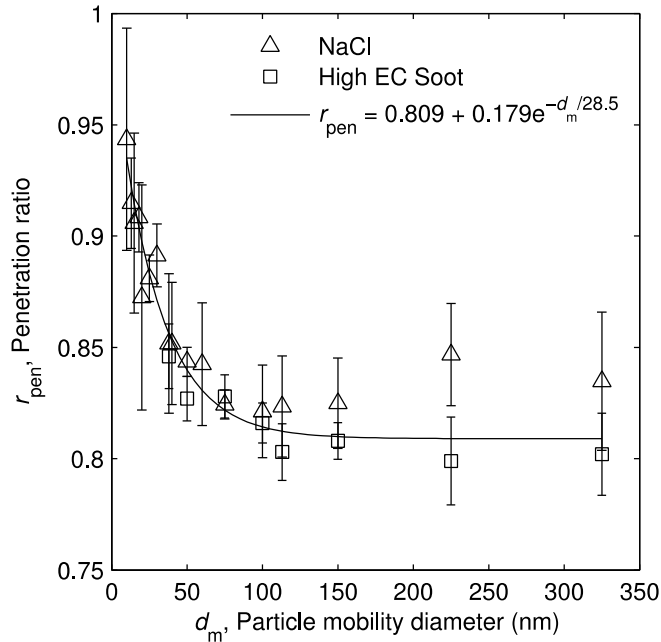


Figure 2.4: Ratio of penetration efficiencies of the hot catalytic denuder over the cold denuder, versus particle mobility diameter. Error bars represent 95% confidence intervals from approximately 10 measurements per data point.

The results of these measurements are shown in Figure 2.4, which shows the ratio of the penetration efficiencies of the hot and cold denuders, against the particle mobility diameter. The test aerosols agree within error estimates, with the exception of the point at 225 nm, and both show an initial decrease followed by the penetration ratio being independent of mobility diameter. (This is more pronounced with the salt, for which we were able to take more measurements at small particle sizes.) Furthermore, because r_{pen} becomes constant at higher particle sizes, corrections for multiply charged particles are not required. The larger multiply charged particles are attenuated by the same amount so that no distortion of the penetration ratio occurs. At smaller sizes, the size dependence of the penetration ratio could cause multiply charged particles to distort the measurements, however there the fraction of multiply charged particles is smaller than the uncertainty of the measurement. To capture the behaviour of the penetration ratio, a best fit exponential curve was found via error normalized residuals minimization. A similar trend in ratios of penetration efficiencies has been found in other studies (e.g. Graves (2015) using a thermodenuder). Penetration efficiencies of the hot and cold denuder can differ due to differences in particle diffusion and thermophoretic losses due to changes in gas viscosity, particle slip correction factor, gas velocity, and temperature gradients.

2.2.3.2 Calculation of Externally Mixed Volatile Particle Fraction

With the penetration ratio characterized, the volatile particle fraction may be calculated from the ratio of the denuded and undenuded number concentrations, correcting for the differences in the losses,

$$f_{vp}(d_m) = 1 - \frac{n_{D,s}(d_m)}{r_{pen}(d_m) n_{U,s}(d_m)} \quad (2.4)$$

where f_{vp} is the volatile particle fraction; and $n_{D,s}$ and $n_{U,s}$ are the measured number concentrations for the denuded and undenuded soot samples. A suitable best-fit curve may be chosen for the volatile particle fraction, in order to represent it with the simple curve bounded between 0 and 1.

2.2.4 Volatile Mass Fraction

Figure 2.3c shows the experimental setup for measuring the volatile mass fraction. As in the measurement of the volatile particle fraction, the aerosol sample is first classified using a DMA and then it is either denuded or left undenuded. The sample is then sent through a CPMA (Cambustion Ltd.) that classifies only the particles of a narrow range of mass-to-charge ratios around a set point. The resolution of the CPMA quantifies the narrowness of the range of classified mass-to-charge ratios; it is equal to the set point divided by the full-width of this range at half-maximum of the transfer function (i.e. the difference between the maximum and minimum values which are classified with at least 50% efficiency at that set point). The CPMA was operated with a flow rate of 1.5 L/min and a resolution of either 3 or 5 depending on the maximum that could be obtained at the given set point. The CPMA is stepped across a range of mass-to-charge set point covering the range of particles exiting the DMA. Finally, the particle number concentration is determined by the CPC from the flow rate and counts of particles.

The DMA selects by electrical mobility after charging the particles with a low charge state, so that most of the particles are either uncharged or singly charged and a small fraction are multiply charged. The electrical mobility is proportional to the product of mobility and charge, so it may allow multiply-charged particles to pass through which are larger than the singly-charged particles. Similarly, the CPMA selects by mass-to-

charge ratio, so it may allow particles to pass through with twice the charge and twice the mass expected, for example. However, the way that the size of the multiply-charged particles scales with charge, after classification by the DMA, causes particles in each charge state to have a different mass-to-charge ratio so that they may in principal be distinguished by the CPMA.

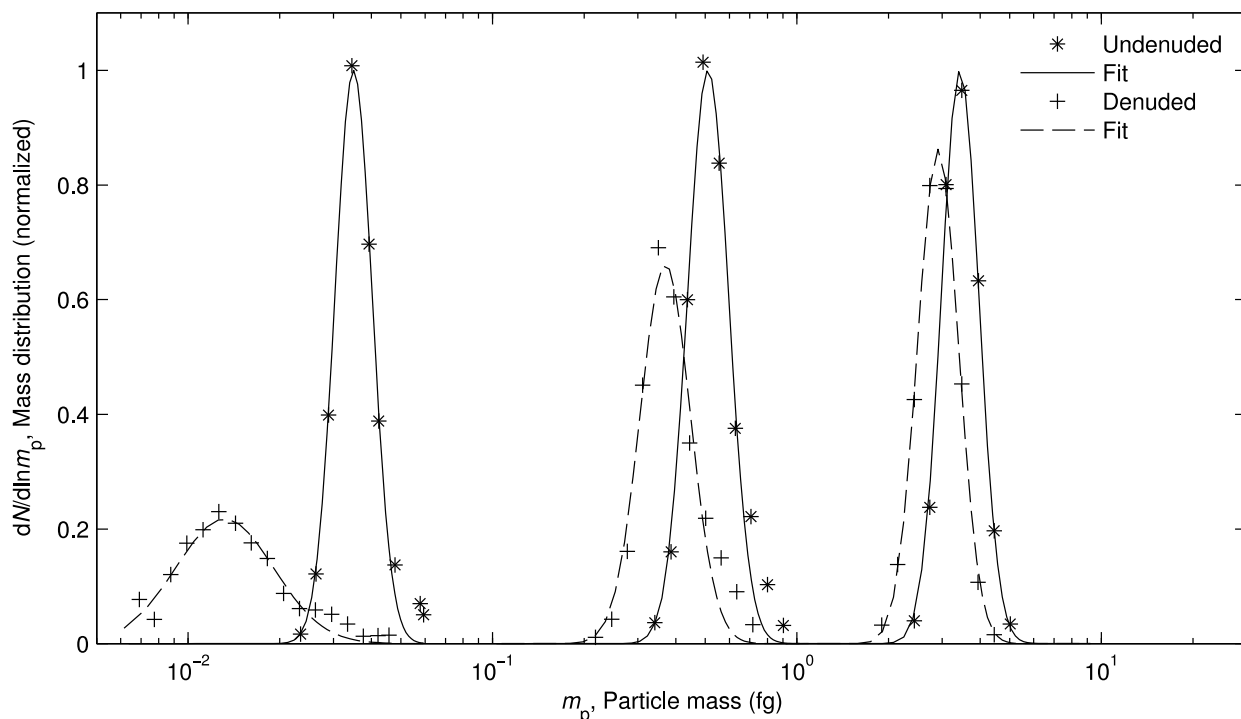


Figure 2.5: Mass distributions (distribution of particle concentration over mass) of size selected soot from the high OC setting, showing how the distribution changes when denuded at DMA set points of 38 nm, 100 nm, and 225 nm (left to right). The median mass of each distribution is determined from a lognormal fit. It can be seen that denuding removes mass from the particles from the shift towards lower median masses.

For the particles of a given mobility size, selected by setting the DMA, the CPMA is scanned over a range of particle masses. This procedure is performed using the hot catalytic denuder and repeated using the cold denuder. By doing this a distribution of the number concentration of particles of each mass is generated, for particles of that size and denuding treatment. Figure 2.5 gives an example of the difference between the mass distributions of undenuded and denuded particles for soot from the high OC setting at three different sizes. The mass distributions are calculated using the inversion routine in the CPMA software (Cambustion CPMA manual). The inversion calculation

depends on the resolution of the CPMA, which is assumed to be constant over the range of masses for each scan. For a given flow rate and geometry of the CPMA (length and radii of cylinders), the resolution is a function of voltage and rotational speed of the CPMA and the mobility of the particles (Olfert & Collings, 2005). Because the particles are classified by mobility in the DMA, for any given CPMA scan the mobility is nearly constant. During a scan the CPMA controls both the rotational speed and voltage which are selected to keep the resolution constant for a given particle mobility, thus an assumption of constant resolution is reasonable. Furthermore, it is assumed that all particles are singly charged. Because the multiply charged particles classified by the DMA typically have a different mass-to-charge ratio than the expected singly charged particles, the presence of a significant number of multiply charged particles would cause additional modes to appear in the mass distribution. The typical distributions in Figure 2.5 show a very slight emergence of a second mode corresponding to the +2 charge state (or higher), causing a bump on the right sides of some of the distributions. However, the bump does not distort the location of the peak of the distributions, nor does it significantly affect the mode determined by a lognormal curve fit, so the effect of multiply-charged particles may be neglected. This assumption is also common in DMA measurements (Stolzenburg & McMurry, 2008). Alternatively, another charge neutralizer can be used before the CPMA to re-neutralize the mobility-classified particles making it easier to distinguish the charge state (Radney and Zangmeister, 2016).

As soot particles have a branched-chain aggregate morphology and are not perfect spheres, there is a range of different masses present at each size. Particles with a more uniform morphology would have a more narrow mass distribution. To simplify calculations to only account for one value of mass at each size, the median mass of the distribution is found using a lognormal approximation, and is taken to represent the mass of particles at that size.⁸ A more nuanced calculation could consider the whole distribution of masses at each size, resulting in a two-dimensional distribution (Ruwata et al., 2016). However, this requires many more measurements and is not expected to

⁸ Because the measured mass distributions are relatively narrow and symmetrical, the median, mean, and mode are expected to be fairly close together; the median was selected for its resistance to outliers.

significantly affect the mass distribution. The difference in the median mass between the undenuded and denuded cases is the internally mixed volatile mass removed by the hot catalytic denuder. Repeating this procedure at different sizes gives the volatile mass fractions, f_{vm} , across the size range of the sample;

$$f_{vm}(d_m) = 1 - \frac{m_D(d_m)}{m_U(d_m)}, \quad (2.5)$$

where d_m is the undenuded particle mobility diameter, m_D is the median mass of the denuded particles, and m_U is the median mass of the undenuded particles. A best-fit curve may be selected to match the volatile mass fraction data with a simple function, keeping in mind that the volatile mass fraction is physically constrained to lie between 0 and 1.

Note that if the densities of the volatile and non-volatile material were sufficiently different, and if there was a sufficient proportion of purely volatile particles, the undenuded mass distribution at each size would show two modes. One would originate from the internally mixed particles with both volatile and non-volatile components, while the other would originate from the purely volatile particles. In our experiment, the proportion of volatile particles was insufficient to produce a noticeable second peak in the mass distribution (see Figure 2.5), which would allow them to be distinguished. Because of this it was assumed that they do not significantly impact the median mass of the distribution. If the situation had been reversed and the proportion of purely volatile particles was very high, it may instead have been that the mode representing the mass of coated particles was indistinguishable. In that case the mass of the externally mixed volatile particles could be found, but the mass of internally mixed particles would be difficult to determine.

Note also that if the aerosol population contained significant amounts of both externally mixed non-volatile material, that is, purely non-volatile particles with no volatile material, and internally mixed particles, this could be detected by comparing the undenuded and denuded mass distributions like those shown in Figure 2.5. If the distributions could be decomposed into the sum of two distributions, one of which maintained a constant

median mass upon denuding (keeping its position on the graph), and one of which reduced its median mass upon denuding (moving left on the graph), this would be evidence of a separation of the non-volatile material into externally and internally mixed states. The peak that did not move would represent the externally mixed non-volatile material, while the peak that moved left would represent the internally mixed non-volatile material. The proportions of these components could be determined by integrating the component distributions. In practice, this would require high CPMA resolution and an effective deconvolution algorithm to determine the component distributions. In the measurements of the miniCAST soot presented here, no such separation of the non-volatile material was observed; either the entire distribution moved (showing all non-volatile material was internally mixed) or it stayed in the same position (externally mixed).

Finally, note that the median mass of the mobility-selected sample is insensitive to particle losses. Since the particles are all roughly the same mobility size, they are all lost at the same rate, so particle losses merely affect the height of the distribution, not the position of the median. Because of this, this measurement is insensitive to the difference in particle losses between the hot catalytic denuder and the cold denuder, unlike the volatile particle number fraction measurement.

2.2.5 Mixing State Mass Distributions

Finally, all these measurements are combined to calculate the mass distributions (distribution of mass over size) of the different material components of the aerosol sample. The externally mixed component (purely volatile particles) has a mass distribution $dM_{\text{ex}}/d \ln d_m$:

$$\frac{dM_{\text{ex}}}{d \ln d_m}(d_m) = m_{\text{vol}}(d_m) f_{\text{vp}}(d_m) \frac{dN}{d \ln d_m}(d_m), \quad (2.6)$$

where $dN/d \ln d_m$ is the size distribution (distribution of particle concentration over size), and m_{vol} is the mass of the independent volatile particles (as a function of size). As noted in section 2.2.4, in our case the volatile particles were not prevalent enough to be able to measure their mass. Instead, it has been assumed that the volatile particles are

spherical with constant density, so that $m_{\text{vol}}(d_m) = \pi d_m^3 \rho_{\text{vol}} / 6$. The density of the volatile material, ρ_{vol} , is assumed to equal to unit density of 1000 kg/m^3 . These assumptions are based on the majority of volatile material being liquid at ambient temperature and pressure, so it can be expected to form into spheres, and furthermore that many volatile organic substances have densities near that of water. Moreover, the mass of the external component is low and so these assumptions do not significantly impact the calculated mass distribution. If there had been a sufficient proportion of purely volatile particles, this mass could have been measured directly.

The internally mixed volatile component and the non-volatile component have mass distributions $dM_{\text{in}}/d \ln d_m$ and $dM_{\text{nv}}/d \ln d_m$, respectively;

$$\frac{dM_{\text{in}}}{d \ln d_m}(d_m) = m_{\text{U}}(d_m) f_{\text{vm}}(d_m) (1 - f_{\text{vp}}(d_m)) \frac{dN}{d \ln d_m}(d_m) \quad (2.7)$$

$$\frac{dM_{\text{nv}}}{d \ln d_m}(d_m) = m_{\text{U}}(d_m) (1 - f_{\text{vm}}(d_m)) (1 - f_{\text{vp}}(d_m)) \frac{dN}{d \ln d_m}(d_m), \quad (2.8)$$

where m_{U} is the median mass of undenuded particles at a given mobility size. These equations extract the number of particles of the given component from the size distribution using the volatile particle fraction, then multiplies that by the mass of the component using the undenuded particle mass and the volatile mass fraction.

The size distributions for the coated non-volatile and purely volatile components can also be calculated from the total size distribution using the volatile particle fraction. For the non-volatile component this is $dN_{\text{nv}}/d \ln d_m$ and for the volatile component this is $dN_{\text{v}}/d \ln d_m$;

$$\frac{dN_{\text{nv}}}{d \ln d_m}(d_m) = (1 - f_{\text{vp}}(d_m)) \frac{dN}{d \ln d_m}(d_m) \quad (2.9)$$

$$\frac{dN_{\text{v}}}{d \ln d_m}(d_m) = f_{\text{vp}}(d_m) \frac{dN}{d \ln d_m}(d_m). \quad (2.10)$$

All of these distributions may be integrated with respect to the logarithm of the particle mobility size to produce the total mass or number concentration of each component, and so the total volatile mass or number fractions can be calculated.

2.3 Results and Discussion

Using the method and experimental setup outlined in Section 2.2, the mixing states of the two miniCAST soot samples were determined. As was expected, the high EC sample had a relatively low amount of volatile material, while the high OC sample had a much more significant proportion of volatile material (see Mamakos et al, 2013).

2.3.1 Volatile Mass Fraction

Figure 2.6 shows the volatile mass fractions of the miniCAST soot at the two different settings.⁹ At high EC, the volatile mass fraction remains very close to zero, averaging only 0.3%. It is practically constant, so its best-fit curve was chosen simply to be the mean of the data points. For soot at high OC, the volatile mass fraction begins at over 60% at small sizes and drops to about 15% at large sizes. This soot has a much larger volatile component than the high EC setting, especially for smaller particles. The volatile mass fraction data for high OC was best fit by a power law. A decreasing trend in volatile mass fraction as a function of mobility-equivalent diameter has also been observed for diesel exhaust (Sakurai et al. 2003; Ristimaki et al. 2007), gasoline direct injection exhaust (Momenimovahed and Olfert, 2015), natural gas direct-injection compression-ignition engine exhaust (Graves et al., 2015), as well as McKenna and inverted burners (Ghazi et al. 2013).

2.3.2 Size Dependence of Particle Mass

Figure 2.7 shows the median masses of the undenuded particles at different sizes. Because of the fractal-like aggregate structure of soot particles, the mass increases by less than the cube of the mobility diameter (this exponent is commonly referred to as the mass-mobility exponent; Sorensen, 2011); this corresponds to larger particles being

⁹ As only one measurement was available for each data point in Figures 2.6 and 2.7, the precision uncertainty could not be determined. Furthermore, the bias uncertainty of the measurements is not relevant as the volatile mass fraction represents a differential measurement. Therefore no error bars are displayed.

less dense with respect to their mobility-equivalent volume. Both sets of data are best fit by a power law. The data shows that soot from the high OC setting is significantly more dense than that from the high EC setting. Presumably, this is due to the volatile material filling voids and producing a particle with a more spherical form.

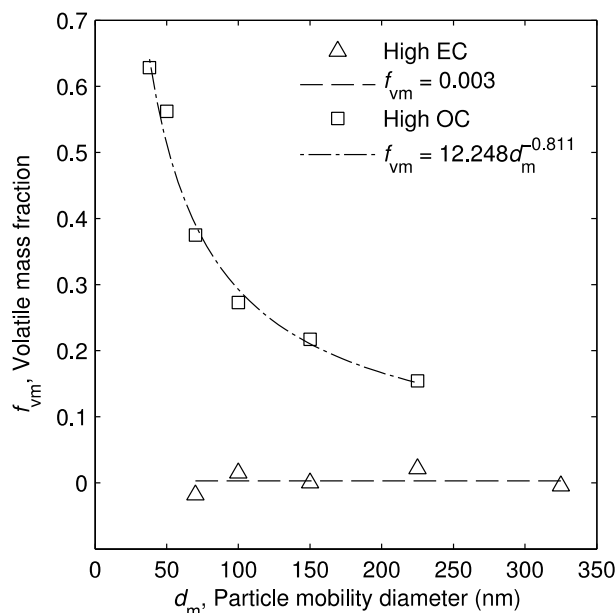


Figure 2.6: Volatile mass fraction versus undenuded particle mobility diameter.

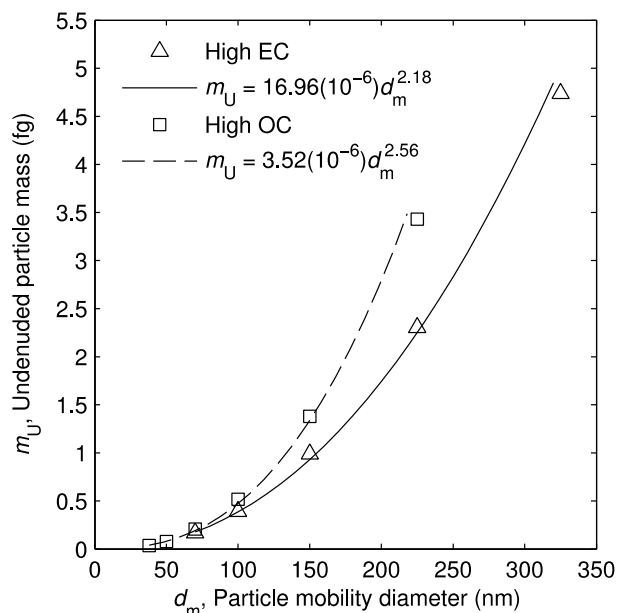


Figure 2.7: Median mass of the undenuded particles versus particle mobility diameter.

2.3.3 Externally Mixed Volatile Particle Fraction

Figure 2.8 shows the volatile particle fractions of the miniCAST soot at the two settings. The error bars in the figure represent 95% confidence intervals on the data points, obtained from between 5 and 10 measurements per data point. The soot generated at the high EC setting has a roughly constant volatile particle fraction around 6%, so it is best fit by its average. This is a small ratio, comparable to the uncertainties, which are also on the order of a few percent for both f_{vp} and r_{pen} (as shown in Figure 2.4). The high OC soot has a high volatile number fraction of over 30% at small particle sizes (< 75 nm), which quickly decreases to roughly the same as the high EC soot. This behaviour is best fit by a decaying exponential.

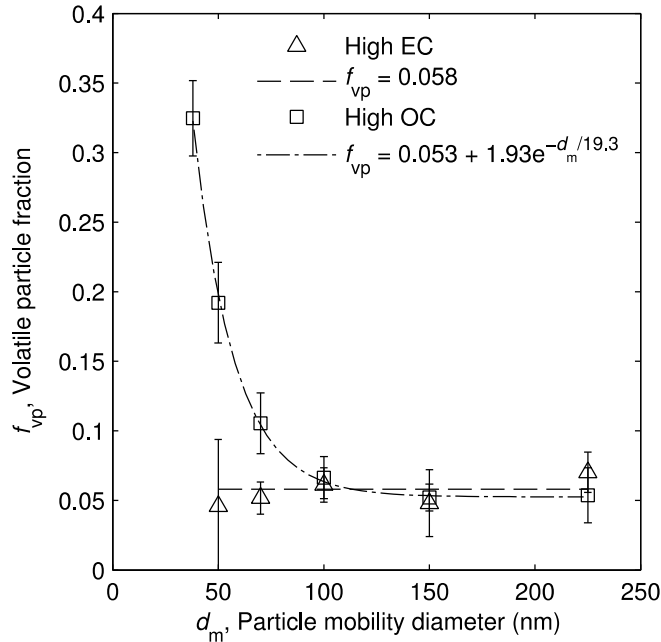


Figure 2.8: Externally mixed volatile particle number fraction versus undenuded particle mobility diameter. Error bars represent 95% confidence intervals from approximately 5 to 10 measurements at each data point.

2.3.4 Mixing State Size and Mass Distributions

Figure 2.9 shows the distribution of number concentration, and Figure 2.10 shows the distribution of mass concentration, over particle mobility diameter and component for the miniCAST soot at a) the high EC setting and b) the high OC setting. These were calculated from the smooth best fit curves from the measurements above. Where data was unavailable, these best fit curves were used for extrapolation (constraining them to lie within physical limits); this extrapolation only occurred at small sizes where the mass is negligible. Note that the curves in Figures 2.9 and 2.10 are additive so the uppermost curve represents the total mass distribution, and the distribution of each component alone is represented by the difference between it and the curve below it. It can be seen how the mass distribution is shifted to the right compared to the number distribution; a greater proportion of the mass is in larger particles.

Numerically integrating the above mass distributions with respect to the logarithm of the mobility diameter produces the total mass concentration of each component, and these can be used to find the total mass fraction of each component. The total mass fractions are summarized in Table 2.2.

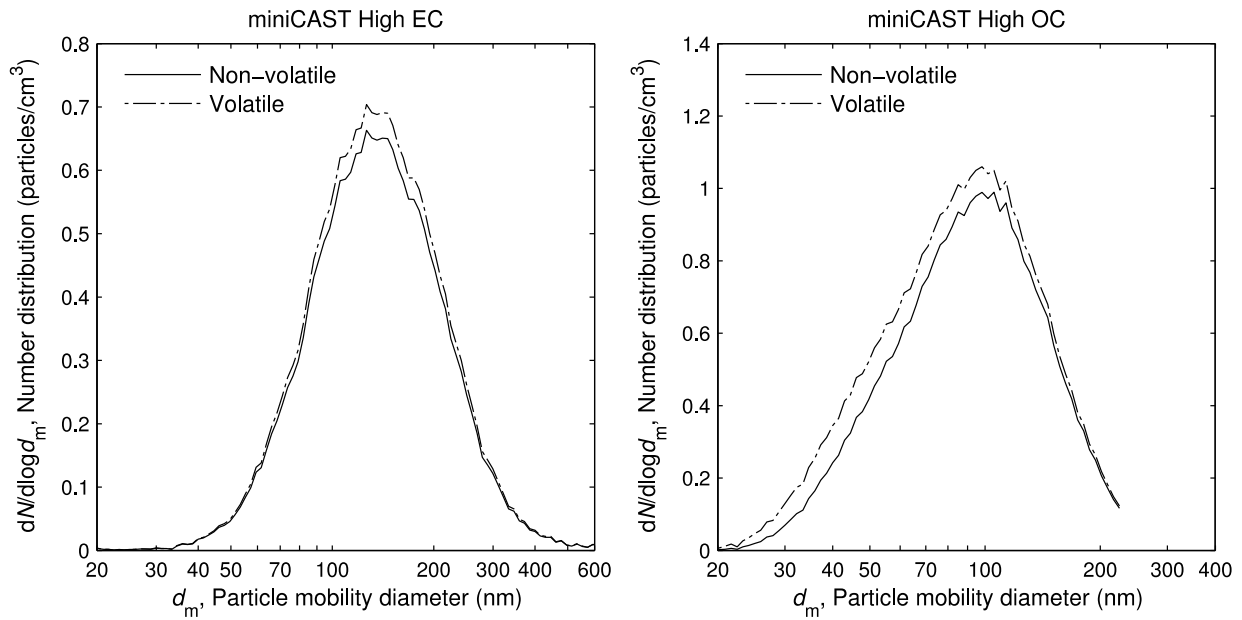


Figure 2.9: Size distributions of the soot from a) high EC and b) high OC showing the number concentration of each component of the sample versus particle mobility diameter. The components are graphed additively; the actual value of each component is given by the difference between its curve and the curve below it.

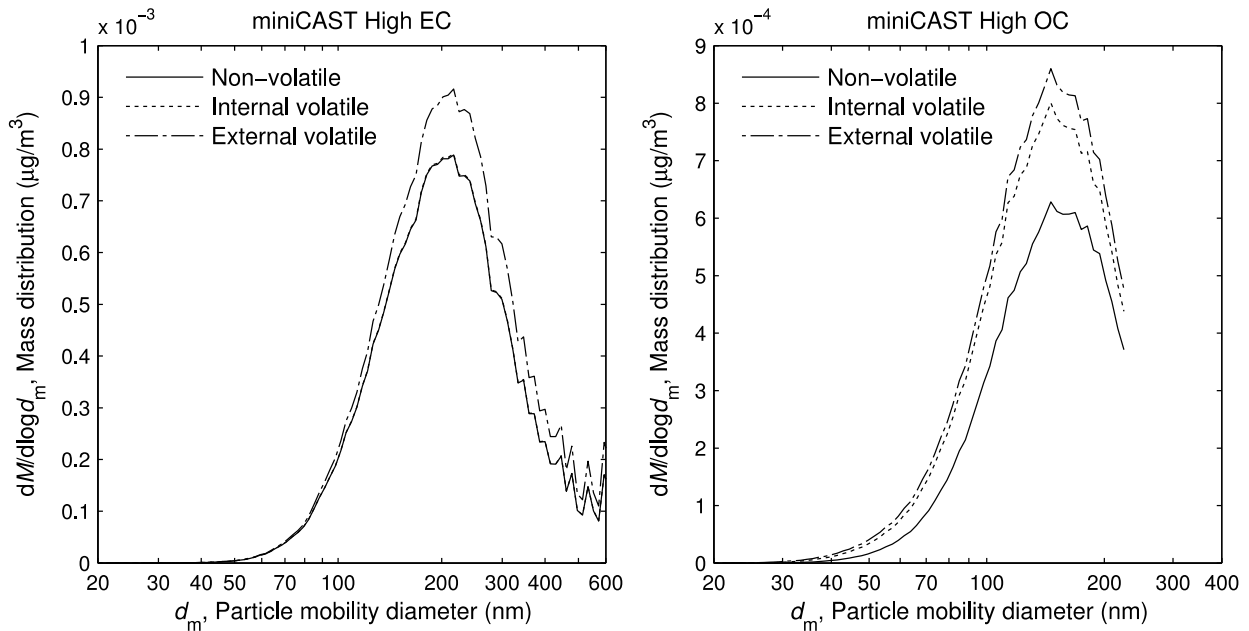


Figure 2.10: Mixing state of the soot from a) high EC and b) high OC. Mass distribution showing the mass concentration of each component of the sample versus particle mobility diameter. As in Figure 2.9, the components are graphed additively.

Table 2.2: Mass fractions of the different material components of the soot from the different set points.

	High EC	High OC
Non-volatile	86%	70%
Internal volatile	0%	22%
External volatile	14%	8%

Uncertainties in these mass concentrations originate from CPMA mass measurement (~3%, Symonds, 2013), DMA size measurement (~3%, Kinney, 1991), and CPC number concentration (~10%, TSI CPC specifications). Combined these give an uncertainty on the order of 16% of the total mass concentration (with 95% confidence) neglecting uncertainty due to the SMPS data inversion, as shown by Momenimovahed et al. (2015).

The soot from the high EC setting is mostly non-volatile, with virtually no internally mixed volatile material at all, and some external volatile particles (around 5% f_{vp}). The irregularity at the upper range of the mass distribution comes from the fact that it represents only a very small number of relatively heavy particles. At that end of the SMPS scan, the concentration measured by the CPC was low enough (<0.01 particles/cm³) that counting statistics were poor, producing a noisy concentration signal. (This can be improved by using a longer SMPS scan time). This is magnified upon weighting by mass. For the high OC setting, the SMPS scan was unable to capture the upper tail of the distribution. The high OC soot has a very significant amount of internally mixed volatile material (22% f_{vm}) to complement its non-volatile component, along with some externally mixed volatile material (around 5% f_{vp} , increasing at lower sizes).

It may be noted that the mass distribution for high EC shows a greater proportion of externally mixed volatile material compared to the distribution for high OC, even though they have very similar volatile particle fractions above 100 nm. This is due to the fact that the density of the purely volatile material is assumed to be constant at 1000 kg/m³, while the density of the non-volatile material is decreasing with size. Thus the particles from high OC are around 750 kg/m³ near the mode of its distribution, and the particles from high EC are only around 450 kg/m³ near the mode of its distribution. The purely

volatile particles therefore form a greater proportion of the mass relative to their number fraction at the high EC condition.

2.4 Conclusion

A methodology to quantify the mixing state of an aerosol with volatile material has been described, and demonstrated using miniCAST-generated soot at high-EC and high-OC settings. The methodology calculates the proportions of aerosol mass at each size which are in each component of the aerosol: non-volatile particles, internally mixed volatile material, and independent volatile particles (externally mixed). In this study, material is considered to be volatile if it is removed by a certain catalytic denuder heated to 350°C; different values for the temperature and residence time of the denuder could produce different results, and this is important to note when comparing these results to others. The mass distribution is found by measuring the volatile mass fractions and volatile number fractions of the aerosol at different sizes, using a DMA to classify by size and a CPMA to classify by mass, and comparing measurements of the sample with and without removing volatile material in a denuder.

The experimental demonstration of this methodology shows that it successfully quantifies the differences between an aerosol with a low amount of independent volatile material, and next to no internally mixed volatile material (the high-EC setting), and an aerosol with a significant amount of volatile material, much of which is internally mixed (the high-OC setting). The method also detects another difference in the morphology of these aerosols, namely that the effective density of the high-OC soot is higher. The method is limited by several factors. To simplify calculations, the method assumes a unique relationship between mass and size, which is valid for particles with a uniform morphology like spheres, but only an approximation for particles like soot. Furthermore, the distribution of masses together with the low number of independent volatile particles in this experiment meant that the density of the volatile material could not be measured, and so a value had to be assumed. In applications with a significant amount of volatile material, the mass of the volatile particles could be directly measured, but in cases with very high proportions of volatile material, the opposite problem could be encountered where it then becomes difficult to measure the mass of the non-volatile particles.

The aerosol used to demonstrate the methodology had internally mixed particles where the volatile material is thought to coat or envelop the non-volatile material, but it is also appropriate for other kinds of internal mixing that may not have a coated structure (e.g. a salt-water aerosol where the non-volatile material dissolves in the volatile material). Furthermore, while it is not observed in the presented data, the method also has the potential to distinguish between different states of non-volatile material when it is present in both externally and internally mixed states. Future work on this methodology could explore these possibilities, and experiment with measuring the mixing states of different kinds of aerosols.

2.5 Bibliography

- China, S., Mazzoleni, C., Gorkowski, K., Aiken, A. C., & Dubey, M. K. (2013). Morphology and mixing state of individual freshly emitted wildfire carbonaceous particles. *Nature Communications*, 4, 2122. <http://doi.org/10.1038/ncomms3122>
- China, S., Scarnato, B., Owen, R. C., Zhang, B., Ampadu, M. T., Kumar, S., ... Mazzoleni, C. (2015). Morphology and mixing state of aged soot particles at a remote marine free troposphere site: Implications for optical properties. *Geophysical Research Letters*, 42(4), 1243–1250. <http://doi.org/10.1002/2014GL062404>
- Cross, E. S., Onasch, T. B., Ahern, A., Wrobel, W., Slowik, J. G., Olfert, J., ... Davidovits, P. (2010). Soot Particle Studies—Instrument Inter-Comparison—Project Overview. *Aerosol Science and Technology*, 44(8), 592–611. Retrieved from <http://dx.doi.org/10.1080/02786826.2010.482113>
- Ehara, K., Hagwood, C., and Coakley, K. J. (1996). Novel Method to Classify Aerosol Particles According to Their Mass-to-Charge Ratio - Aerosol Particle Mass Analyser. *J. Aerosol Sci.*, 27:217–234.
- Ghazi, R., & Olfert, J. S. (2013). Coating Mass Dependence of Soot Aggregate Restructuring due to Coatings of Oleic Acid and Dioctyl Sebacate. *Aerosol Science and Technology* 47(2), 192-200. <http://doi.org/10.1080/02786826.2012.741273>
- Ghazi, R., Tjong, H., Soewono, A., Rogak, S. N., and Olfert, J. S. (2013). Mass, mobility, volatility, and morphology of soot particles generated by a mckenna and inverted burner. *Aerosol Science and Technology*, 47(4), 395-405.
- Graves, B., Olfert, J. S., Patychuk, B., Dastanpour, R. & Rogak, S. (2015). Characterization of Particulate Matter Morphology and Volatility from a Compression-Ignition Natural-Gas Direct-Injection Engine. *Aerosol Science & Technology* 49(8), 589-598. <http://doi.org/10.1080/02786826.2015.1050482>

- Graves, B. (2015). Characterization of Particulate Matter Morphology and Volatility for Two Direct-Injection Engines. MSc. thesis, *Univeristy of Alberta*.
- Jayne, J. T., Leard, D. C., Zhang, X., Davidovits, P., Smith, K. A., Kolb, C. E., & Worsnop, D. R. (2000). Development of an Aerosol Mass Spectrometer for Size and Composition Analysis of Submicron Particles. *Aerosol Science and Technology*, 33(1-2), 49–70. <http://doi.org/10.1080/027868200410840>
- Kinney, P. D., Pui, D. Y. H., Mulholland, G. W., and Bryner, N. P. (1991). Use of the Electrical Classification Method to Size 0.1 μm SRM Particles—A Feasibility Study. *J. Res. Natl. Inst. Stan. Technol.*, 96:147–176.
- Knutson, E. O. and Whitby, K. T. (1975). Aerosol Classification by Electric Mobility: Apparatus, Theory, and Application, *J. Aerosol Sci.* 6:443–451
- Kuwata, M., Kondo, Y., & Takegawa, N. (2009). Critical condensed mass for activation of black carbon as cloud condensation nuclei in Tokyo. *Journal of Geophysical Research*, 114(D20), D20202. <http://doi.org/10.1029/2009JD012086>
- Lee, A. K. Y., Willis, M. D., Healy, R. M., Onasch, T. B., & Abbatt, J. P. D. (2015). Mixing state of carbonaceous aerosol in an urban environment: single particle characterization using the soot particle aerosol mass spectrometer (SP-AMS). *Atmospheric Chemistry and Physics*, 15(4), 1823–1841. <http://doi.org/10.5194/acp-15-1823-2015>
- Mamakos, A., Khalek, I., Giannelli, R. & Spears, M. (2013). Characterization of Combustion Aerosol Produced by a Mini-CAST and Treated in a Catalytic Stripper. *Aerosol Science & Technology* 47(8), 927-936. doi: 10.1080/02786826.2013.802762
- McMeeking, G. R., Morgan, W. T., Flynn, M., Highwood, E. J., Turnbull, K., Haywood, J., & Coe, H. (2011). Black carbon aerosol mixing state, organic aerosols and aerosol optical properties over the United Kingdom. *Atmospheric Chemistry and Physics*, 11(17), 9037–9052. <http://doi.org/10.5194/acp-11-9037-2011>
- Momenimovahed, A. & Olfert, J. S. (2015). Effective Density and Volatility of Particles Emitted from Gasoline Direct Injection Vehicles and Implications for Particle Mass Measurement. *Aerosol Science & Technology* 49(11), 1051-1062. <http://doi.org/10.1080/02786826.2015.1094181>
- Moteki, N., & Kondo, Y. (2007). Effects of Mixing State on Black Carbon Measurements by Laser-Induced Incandescence. *Aerosol Science and Technology*, 41(4), 398–417. <http://doi.org/10.1080/02786820701199728>
- Olfert, J. S., & Collings, N. (2005). New method for particle mass classification—the Couette centrifugal particle mass analyzer. *Journal of Aerosol Science*, 36(11), 1338–1352. <http://doi.org/10.1016/j.jaerosci.2005.03.006>
- Onasch, T. B., Trimborn, A., Fortner, E. C., Jayne, J. T., Kok, G. L., Williams, L. R., ... Worsnop, D. R. (2012). Soot Particle Aerosol Mass Spectrometer: Development, Validation, and

- Initial Application. *Aerosol Science and Technology*, 46(7), 804–817.
<http://doi.org/10.1080/02786826.2012.663948>
- Pagels, J., Khalizov, A. F., McMurry, P. H., & Zhang, R. Y. (2009). Processing of Soot by Controlled Sulphuric Acid and Water Condensation—Mass and Mobility Relationship. *Aerosol Science and Technology*, 43(7), 629–640.
<http://doi.org/10.1080/02786820902810685>
- Petzold, A., Ogren, J., Fiebig, M., Laj, P., Li, S.-M., Baltensperger, U., ... Zhang, X.-Y. (2013). Recommendations for reporting "black carbon" measurements. *Atmospheric Chemistry and Physics*, 13, 8365-8379. doi:10.5194/acp-13-8365-2013
- Radney, J. G. and Zangmeister, C. D. (2016). Practical limitations of aerosol separation by a tandem differential mobility analyzer-aerosol particle mass analyzer. *Aerosol Science and Technology*. doi: 10.1080/02786826.2015.1136733
- Rawata, V. K., Buckleya, D. T., Kimotoa, S., Leeb M.-H., Fukushimac, N., Hogan, C. J. (2016). Two dimensional size–mass distribution function inversion from differential mobility analyzer–aerosol particle mass analyzer (DMA–APM) measurements. *Journal of Aerosol Science* 92, 70-82. doi:10.1016/j.jaerosci.2015.11.001
- Rissler, J., Nordin, E., Eriksson, A., Nilsson, P., Frosch, M., Sporre, M., ... Swietlicki, E. (2014). Effective Density and Mixing State of Aerosol Particles in a Near-Traffic Urban Environment. *Environ. Sci. Technol.*, 48 (11), pp 6300–6308. doi: 10.1021/es5000353
- SAE. (2013). Aerospace Information Report (AIR) 6241, Procedure for the Continuous Sampling and Measurement of Non-Volatile Particle Emissions from Aircraft Turbine Engines. *SAE International*, Warrendale, PA
- Sakurai, H., Park, K., McMurry, P. H., Zaring, D. D., Kittleson, D. B., and Ziemann, P. J. (2003). Size-Dependent Mixing Characteristics of Volatile and Nonvolatile Components in Diesel Exhaust Aerosols. *Environ. Sci. Technol.*, 37:5487–5495.
- Schnitzler, E., Dutt, A., Charbonneau, A., Olfert, J. S., and Jaeger, W. (2014) Soot aggregate restructuring due to coatings of secondary organic aerosols derived from aromatic precursors. *Environmental Science & Technology*, 48:14309-14316.
- Schwarz, J. P., Spackman, J. R., Gao, R. S., Perring, A. E., Cross, E., Onasch, T. B., Ahern, A., Wrobel, W., Davidovits, P., Olfert J., Dubey, M. K., Mazzoleni C. & Fahey D. W. (2010). The Detection Efficiency of the Single Particle Soot Photometer. *Aerosol Science and Technology*, 44(8), 612-628. <http://doi.org/10.1080/02786826.2010.481298>
- Sorensen, C. M. (2011) The Mobility of Fractal Aggregates: A Review. *Aerosol Science & Technology* 45(7), 765-779. doi: 10.1080/02786826.2011.560909
- Stephens, M., Turner, N., & Sandberg, J. (2003). Particle Identification by Laser-Induced Incandescence in a Solid-State Laser Cavity. *Applied Optics*, 42(19), 3726.
<http://doi.org/10.1364/AO.42.003726>

- Stolzenburg, M. R., & McMurry, P. H. (2008). Equations Governing Single and Tandem DMA Configurations and a New Lognormal Approximation to the Transfer Function. *Aerosol Science and Technology*, 42(6), 421–432. <http://doi.org/10.1080/02786820802157823>
- Swanson, J.J., & Schulz, H.-J. (2013). “Measurement of solid particle concentration is aided by catalytic stripper technology”. Poster presented at *European Aerosol Conference 2013*.
- Symonds, Jonathan P. R., Reavell, Kingsley St.J., and Olfert, Jason S. (2013). The CPMA-electrometer system - A suspended particle mass concentration standard. *Aerosol Science and Technology*, 47(8):i-iv.
- UNECE Regulation No. 83 (Emissions of M1 and N1 categories of vehicles). Available at: <http://www.unece.org/trans/main/wp29/wp29regs81-100.html>
- Wang, Q., Huang, R.-J., Cao, J., Han, Y., Wang, G., Li, G., ... Zhou, Y. (2014). Mixing State of Black Carbon Aerosol in a Heavily Polluted Urban Area of China: Implications for Light Absorption Enhancement. *Aerosol Science and Technology*, 48(7), 689–697. <http://doi.org/10.1080/02786826.2014.917758>
- Wang, S. C., & Flagan, R. C. (1990). Scanning Electrical Mobility Spectrometer. *Aerosol Science and Technology*, 13(2), 230–240. <http://doi.org/10.1080/02786829008959441>
- Zhang, R., Khalizov, A. F., Pagels, J., Zhang, D., Xue, H., & McMurry, P. H. (2008). Variability in morphology, hygroscopicity, and optical properties of soot aerosols during atmospheric processing. *Proceedings of the National Academy of Sciences of the United States of America*, 105(30), 10291–6. Retrieved from <http://www.pnas.org/cgi/content/abstract/105/30/10291>

3. Mixing State of Particles Emitted from a Gas Turbine Engine¹

In this chapter we present size-segregated measurements of the mixing state of soot from a Rolls-Royce Gnome turbine engine, at two engine settings: high power (22,000 RPM) and low power (13,000 RPM). The mass distributions of the non-volatile, internally mixed volatile, and externally mixed volatile components of the aerosol are calculated. From these measurements, the relative proportions of these different components can be extracted for particles at different mobility diameters. The effective densities of the sample aerosols are also measured, and compared with soot from other aircraft gas turbine engine sources.

3.1 Experimental Setup

Studies have been done on the volatility of particles through various techniques, including single particle techniques and population average techniques. Single particle techniques include scanning electron microscopy (China et al., 2015; China et al., 2013), particle mass spectroscopy (Cross et al., 2010; Onasch et al., 2012), and combined measurements of particle scattering and incandescence (McMeeking et al., 2011; Moteki & Kondo, 2007). However, these are limited either by the inability to quantitatively differentiate volatile from non-volatile material, or because they can only detect relatively large particles (Schwarz et al., 2010, Wang et al., 2014, Lee et al., 2015). Population based techniques include chemical EC/OC analysis (NIOSH 2003) and tandem differential mobility analyser techniques (Petzold et al 2005). In this chapter we quantify the mixing state of Gnome turbine engine particulate by calculating mass distributions of the different components of the particulate (non-volatile and internally and externally mixed volatile) from measurements of the number distribution and the volatile number and mass fractions. This is done following the methodology of Chapter 2, which is summarized here.

¹ A version of this chapter is being prepared for submission for publication as Dickau, M., Olfert, J., Momenimovahed, A., Thomson, K., Smallwood, G., Stettler, M., Boies, A., Johnson, M. (2016) Mixing State of Particles Emitted from a Gas Turbine Engine. *Atmospheric Environment*.

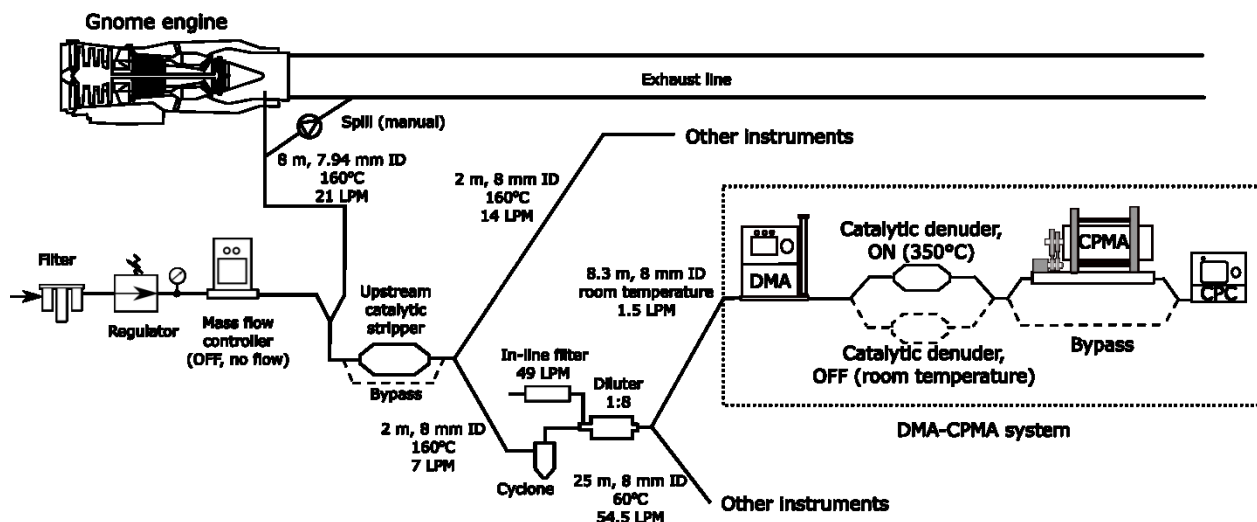


Figure 3.1: Experimental setup for measurements of the volatile mass fraction and volatile particle number fraction, showing the sampling system and the DMA-CPMA setup.

Figure 3.1 shows the experimental setup used to measure the volatile mass fractions and volatile particle fractions of the soot sample. These measurements were performed as part of a larger campaign and other instruments not relevant to this work are not shown. An 8-meter sample line at 160°C was used to transfer the aerosol from the Gnome engine exhaust to a 2-way splitter where particle-free dilution air could be introduced into the sample if desired in order to decrease the particle concentration. For all measurements presented in this work, no make-up air was introduced at this stage. A catalytic stripper was placed upstream of the measurement system. For all measurements of volatility presented in this work, this upstream catalytic stripper was either off or bypassed entirely. Only in the case of certain non-volatile particle measurements, the upstream CS was set to 350°C to remove volatile material prior to measurement. A second heated sample line transferred the aerosol from the upstream CS to a diluter (dilution ratio 1:8). In order to remove relatively larger particles from the sample, a 1 micron sharp cut cyclone was employed upstream of the diluter. After this, a 2-way splitter provided sample for the DMA-CPMA system, as well as other instruments.

In the DMA-CPMA system, the sample aerosol is sent to a differential mobility analyzer (DMA; model 3081, TSI Inc.), which classifies the sample by electrical mobility. The DMA classifies a narrow range of singly-charged particles near the mobility diameter of

choice (25 to 250 nm in this study) as well as larger multiply-charged particles with the equivalent electrical mobility. In this study, the fraction of multiply-charged particles is relatively small as the median mobility diameter for the two engine conditions were 38 and 71 nm. From the DMA, the soot sample is then sent through either a catalytic denuder (Model CS015; Catalytic Instruments) heated to 350 °C, or through an inactive denuder (Model CS015; Catalytic Instruments) at ambient temperature. The hot denuder removes volatile material from the sample, while the cold denuder leaves the sample unchanged. (According to our operational definition of volatility, the volatile material is precisely the material which is removed at 350 °C in the hot catalytic denuder.)

To measure the volatile mass fraction, the particles are then sent through the centrifugal particle mass analyzer (Cambustion Ltd), which classifies the sample by mass-to-charge ratio, and finally the number concentration of the particles is measured with a condensation particle counter (CPC; model 3776, TSI Inc.) with an aerosol flow of 1.5 L/min. The CPMA is scanned over a range of mass set points to determine the number of particles present at different masses at the specific mobility selected by the DMA; this data is used to determine the median mass of particles at the DMA mobility-equivalent diameter. The volatile mass fraction is defined as the fraction of volatile material contained in the particle,

$$f_{vm}(d_m) = 1 - \frac{m_D(d_m)}{m_U(d_m)}, \quad (3.1)$$

where d_m is the particle mobility diameter, m_D is the median mass of the denuded particles, and m_U is the median mass of the undenuded particles.

To measure the volatile particle number fraction, the soot is sent through the bypass line instead of the CPMA, and the number concentration is measured by the CPC. The volatile particle fraction (f_{vp}) is the fraction of particles in the aerosol that are only comprised of volatile material, and is calculated for each particle size selected by the DMA by comparing the number concentrations of the denuded and undenuded soot;

$$f_{vp}(d_m) = 1 - \frac{n_{D,s}(d_m)}{r_{pen}(d_m) n_{U,s}(d_m)} \quad (3.2)$$

where $n_{D,s}$ and $n_{U,s}$ are the measured number concentrations for the denuded and undenuded soot samples, and r_{pen} is the ratio of the penetration efficiency of the hot catalytic denuder to the penetration efficiency of the ambient temperature catalytic denuder. In order to do this accurately, the differences in penetration losses between the hot and cold denuders had to be characterized; this is done in Chapter 2.

For both the volatile mass fraction and the volatile number fraction, additional measurements were made with the upstream catalytic stripper turned on, in order to remove all volatile material before measurement to determine the effective density of only the non-volatile (soot) component of the aerosol. In theory, these denuded measurements should show no volatile material present.

The number distribution was also measured using a scanning mobility particle sizer: differential mobility analyzer (DMA; model 3081, TSI Inc.) with sheath flow of 15 L/min and a condensation particle counter (CPC; model 3776, TSI Inc.) with an aerosol flow of 1.5 L/min. The size distribution is calculated from this data using the inversion routine in the TSI AIM software (version 9).

3.2 Results

3.2.1 Effective Density

Figure 3.2 shows the effective density measurements for the Gnome engine particulate at the 22,000 RPM and 13,000 RPM settings. In both cases, measurements were done for both the undenuded sample (both volatile and non-volatile material present) and the denuded sample (volatile material removed by catalytic denuder upstream of the DMA). For the 22,000 RPM setting, the denuded measurements overlap with the undenuded measurements, showing that the removal of volatile material has a negligible effect on the effective density. The fit curve for the effective density ($\rho_{eff} = C d_m^{-n}$) of undenuded particles at 22,000 RPM was found to be $n = 0.388$, $C = 3046.4 \text{ kg m}^{-3} \text{ nm}^{0.388}$, with $R^2 = 0.9481$. For the 13,000 RPM setting, the denuded measurements are around 5% to 15% lower than the undenuded measurements, showing that there is a reduction in the

effective density of the particles due to removal of volatile material which presumably fills the voids in the soot (increasing particle mass with little change in the particle mobility). The effective density values of undenuded particles at 13,000 RPM lay on a fit curve with $n = 0.560$, $C = 6556.0 \text{ kg m}^{-3} \text{ nm}^{0.560}$, with $R^2 = 0.9993$. For the undenuded data, the particles at 13,000 RPM are slightly denser than the particles at 22,000 RPM across the size range where they may be compared. For the denuded data, the situation is reversed, and the particles from 22,000 RPM are slightly denser.

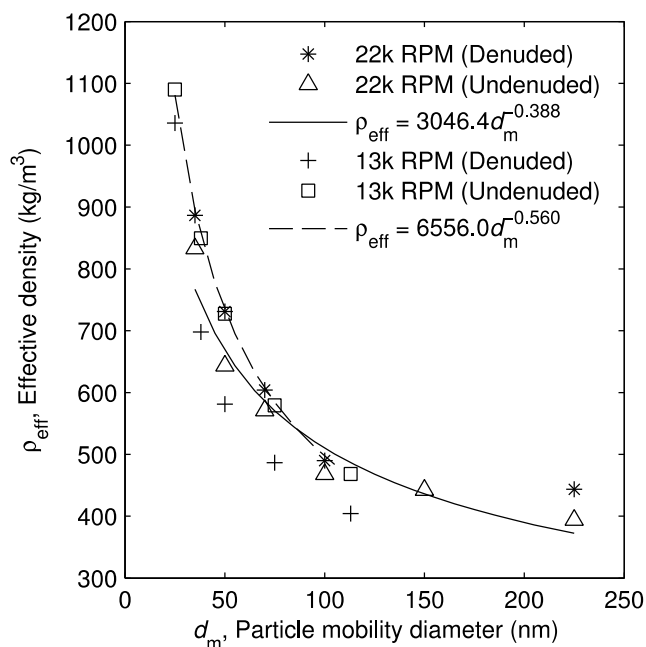


Figure 3.2: Effective density versus particle mobility diameter for particles from a Gnome engine at 22,000 RPM and 13,000 RPM, with and without a denuder placed upstream of the DMA. The best-fit lines for the undenuded measurements are shown.

Figure 3.3 shows a comparison of the effective densities measured for denuded soot from the Gnome engine to that of denuded soot from a CFM56-5B4/2P turbine (Johnson et al. 2013). The shaded region represents the fit range given by Johnson. Here it can be seen that the measured densities are fairly similar. The densities measured for the Gnome engine decrease with increasing mobility diameter faster than Johnson’s data; however, they agree to within approximately 20%. This indicates a similarity between the morphologies of the non-volatile particulates of these engines.

Figure 3.4 shows a comparison of the effective densities measured for undenuded soot from the Gnome engine to that of undenuded soot from a CFM56-5B4/2P (Lobo et al. 2015) and a CFM56-7B26/3 (Abegglen et al. 2015, Durdina et al. 2014). The dark shaded region is the range bounded by Abegglen’s fit curves from 22% engine thrust

(lower boundary) to 118% thrust (upper boundary). The light shaded region is the range bounded by Durdina's fit curves from 3%-5% thrust (lower boundary) to 50%-100% thrust (upper boundary). Lobo's data is close to the measurements from the Gnome engine. Abegglen's and Durdina's data overlap each other significantly, and for the most part they lie significantly above the measurements from the Gnome engine. This indicates that the particulates from this engine have greater density than the particulates from the Gnome engine, when both non-volatile and volatile components are considered. This may be due to a greater proportion of volatile material, filling voids in the soot to increase density without noticeably changing the mobility diameter (Ghazi et al. 2013). The fact that Abegglen and Durdina measured the effective density using undiluted sample may also contribute to the higher density, as this would increase condensation of volatile material.

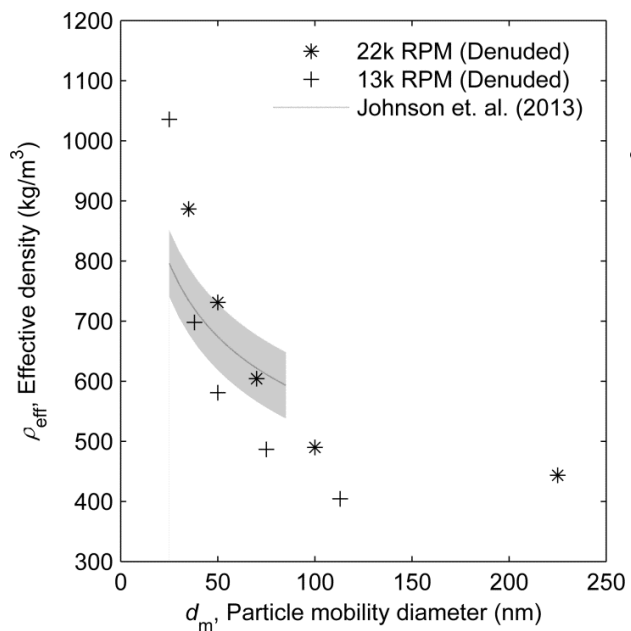


Figure 3.3: Comparison of the effective densities of denuded Gnome engine particulate to that of a CFM56-5B4/2P turbine (Johnson et al. 2013).

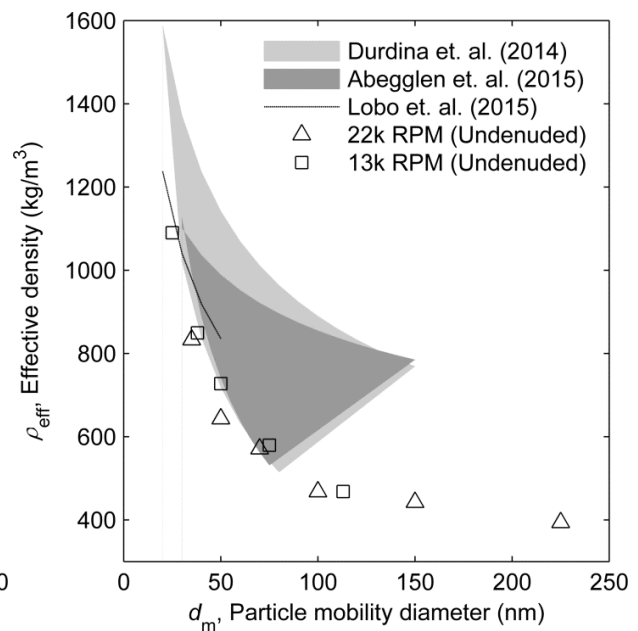


Figure 3.4: Comparison of the effective densities of undenuded Gnome engine particulate to that of a CFM56-5B4/2P turbine (Lobo et al. 2015) and a CFM56-7B26/3 (Abegglen et al. 2015, Durdina et al. 2014).

3.2.2 Volatile Mass Fraction

Figure 3.5 shows the volatile mass fractions of the Gnome engine soot, at 22,000 RPM and 13,000 RPM. Enough data was available for the 13,000 RPM setting to calculate 95% confidence intervals for the values, which are shown. At 13,000 RPM, the soot has volatile mass fractions in the range of 6-12%, gradually decreasing with increasing size. The soot at 22,000 RPM has volatile mass fractions ranging around 1-5%. The large confidence intervals for the 13,000 RPM volatile mass fractions (that span a range of over 0.10) is due to variability in the volatile mass fraction of that operating condition which was measured over several days and also due to measurement uncertainty. A decreasing trend in volatile mass fraction as a function of mobility-equivalent diameter has also been observed for particulate from diesel engines (Sakurai et al. 2003; Ristimaki et al. 2007), gasoline direct injection engines (Momenimovahed and Olfert, 2015), natural gas direct-injection compression-ignition engines (Graves et al., 2015), as well as pre-mixed flames (e.g. McKenna burner; Ghazi et al. 2013) and diffusion flames (e.g. mini-CAST; as seen in Chapter 2).

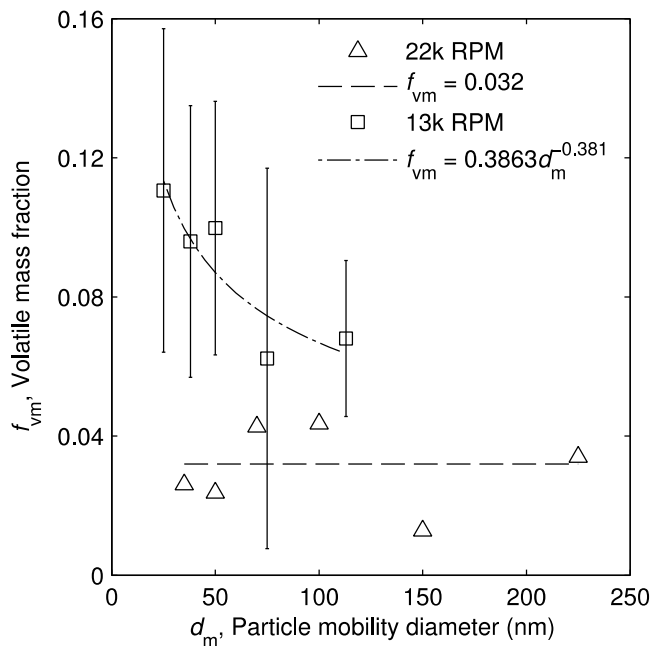


Figure 3.5: Volatile mass fraction versus particle mobility diameter for particulate from a Gnome engine at 22,000 RPM and 13,000 RPM. The error bars on the 13,000 RPM data points represent 95% confidence intervals, from approximately 5 measurements per data point.

3.2.3 Volatile Particle Number Fraction

Figure 3.6 shows the volatile number fractions of the Gnome engine soot, at 22,000 RPM and 13,000 RPM. The error bars represent 95% confidence intervals on the measurements. The soot at 22,000 RPM has volatile number fractions around 5-10%, showing a slight decrease with increasing particle size. For the soot at 13,000 RPM, the volatile number fraction was over 40% for very small particles, decreasing down to around 5% for large particles.

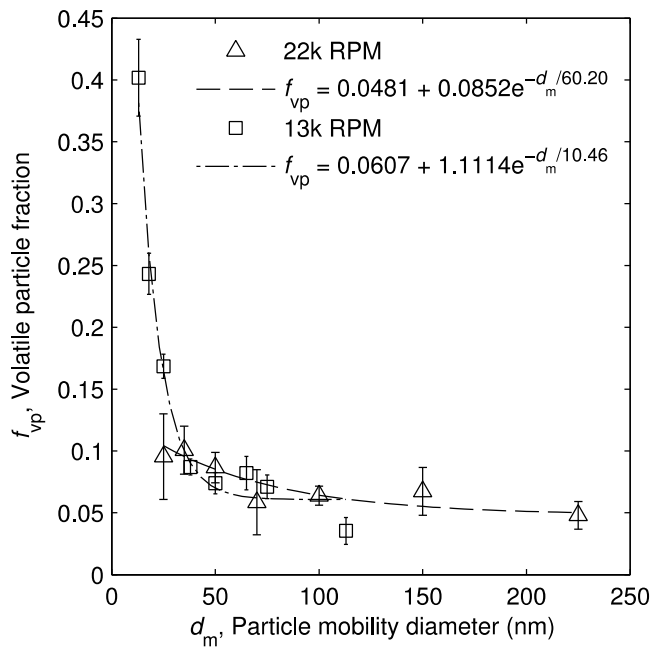


Figure 3.6: Volatile particle number fraction particle mobility diameter for particulate from a Gnome engine at 22,000 RPM and 13,000 RPM. The error bars represent 95% confidence intervals, from approximately 10 measurements per data point.

3.2.4 Size and Mass Distributions

Figure 3.7 shows the number distributions, and Figure 3.8 shows the mass distributions over particle mobility diameter for the Gnome engine particulate at a) the 13,000 RPM setting and b) the 22,000 RPM setting. These distributions are calculated from the total size distribution measured by the SMPS, $dN/d \ln d_m$, the volatile fractions described above (f_{vp} and f_{vm} as shown in Figure 3.5 and 3.6) and, for mass distributions, the mass of the particles from the effective density measurement (shown in Figure 2).

Specifically, the number distribution of particles that contain a non-volatile component, $dN_{nv}/d \ln d_m$, is;

$$\frac{dN_{nv}}{d \ln d_m}(d_m) = (1 - f_{vp}(d_m)) \frac{dN}{d \ln d_m}(d_m) \quad (3.3)$$

and the number distribution of particles that are solely volatile, $dN_v/d \ln d_m$, is;

$$\frac{dN_v}{d \ln d_m}(d_m) = f_{vp}(d_m) \frac{dN}{d \ln d_m}(d_m). \quad (3.4)$$

Similarly, the mass distribution of the non-volatile component of the aerosol is;

$$\frac{dM_{nv}}{d \ln d_m}(d_m) = (1 - f_{vm}(d_m)) \frac{\pi}{6} d_m^3 \rho_{\text{eff}}(d_m) (1 - f_{vp}(d_m)) \frac{dN}{d \ln d_m}(d_m) \quad (5)$$

where the term $\frac{\pi}{6} d_m^3 \rho_{\text{eff}}(d_m)$ is the median mass of the internally mixed particles. The mass distribution of the internally mixed volatile component of the aerosol is,

$$\frac{dM_{in}}{d \ln d_m}(d_m) = f_{vm}(d_m) \frac{\pi}{6} d_m^3 \rho_{\text{eff}}(d_m) (1 - f_{vp}(d_m)) \frac{dN}{d \ln d_m}(d_m) \quad (6)$$

And the mass distribution of the externally mixed volatile is,

$$\frac{dM_{ex}}{d \ln d_m}(d_m) = \frac{\pi}{6} d_m^3 \rho_{\text{vol}} f_{vp}(d_m) \frac{dN}{d \ln d_m}(d_m) \quad (7)$$

where the term $\frac{\pi}{6} d_m^3 \rho_{\text{vol}}$ is the mass of the externally mixed particles. Theoretically, the mass of the externally mixed particles would be measured in the DMA-CPMA system. However, if the concentration of externally mixed particle is small with respect to the concentration of the internally mixed particles (which is the case here) or if the effective densities of the internally and externally mixed particle is similar, then the mass of the externally mixed particles cannot be resolved with the DMA-CPMA system (see Dickau et al. 2016 for details). Therefore, we have assumed that the density of the externally mixed particles is 1000 kg/m^3 as the volatile material is likely organic carbon.

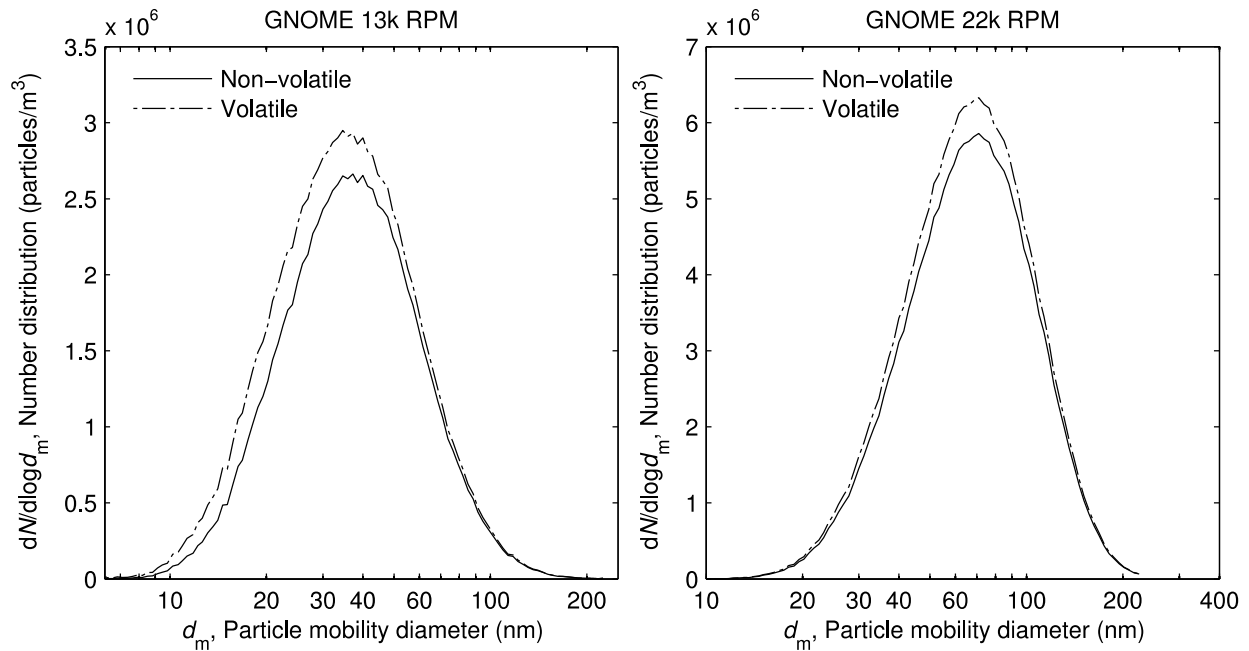


Figure 3.7: Number distributions of Gnome engine particulate from a) the 13,000 RPM condition and b) the 22,000 RPM condition, showing the number concentration of each component (volatile and non-volatile) at different particle mobility diameters. The components are graphed additively; the actual value of each component is given by the difference between its curve and the curve below it.

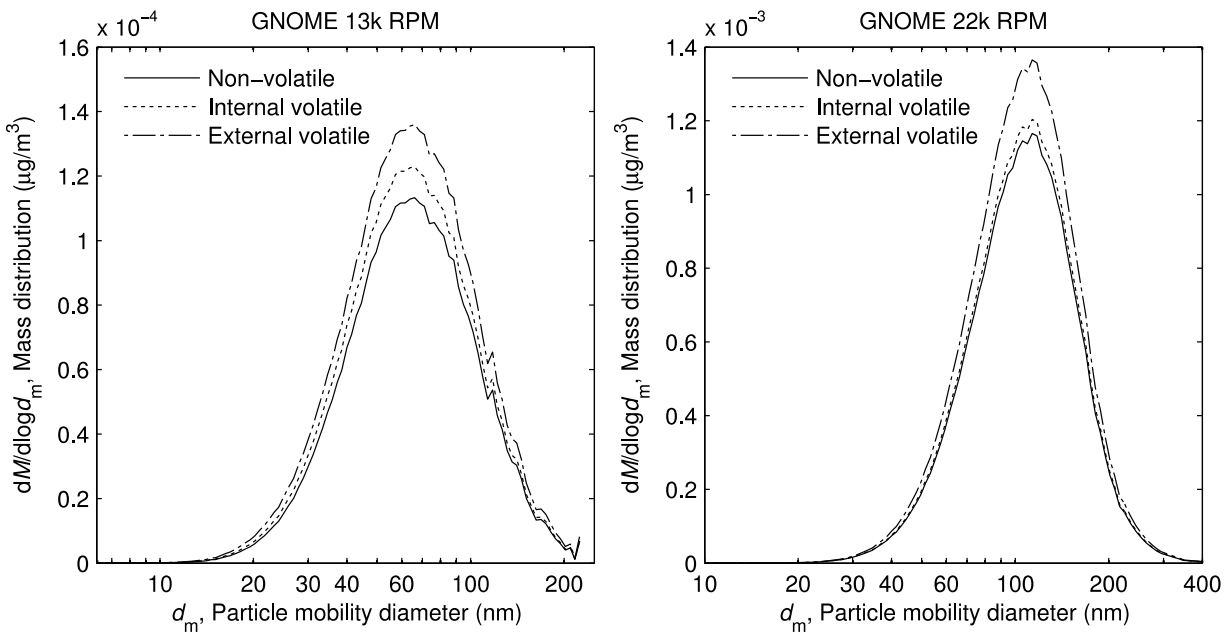


Figure 3.8: Mass distributions of Gnome engine particulate from a) the 13,000 RPM condition and b) the 22,000 RPM condition, showing the mass concentration of each component (non-volatile, internally mixed volatile, and externally mixed volatile) at different particle mobility diameters. As in Figure 3.7, the components are graphed additively.

Note that the curves in Figures 3.7 and 3.8 are additive so the uppermost curve represents the total mass distribution, and the distribution of each component alone is represented by the difference between it and the curve below it. The mass median diameters of the overall mass distributions are 107 nm for the 22,000 RPM setting (geometric standard deviation (GSD) of 1.46), and 65 nm for the 13,000 RPM setting (GSD 1.59). These are different from the count median diameters (71 nm and 38 nm, respectively) because the distribution is being weighted by mass rather than particle number.

Table 3.1: Total mass fractions for the different components of the particulate at different engine conditions

	22,000 RPM	13,000 RPM
Non-volatile	85%	82%
Internal volatile	3%	7%
External volatile	12%	11%

These curves can be integrated to give the total mass fractions for each component of the soot, as shown in Table 3.1. Both mass distributions show that the majority of the mass of the soot is in the non-volatile component. Furthermore, the particulate from the 22,000 RPM setting shows only a very small proportion (3% by mass) of internally mixed volatile material. There is a noticeable amount of externally mixed volatile material at both engine conditions. For the 13,000 RPM setting, there is a noticeable amount (7% by mass) of internally mixed volatile material, and again some purely volatile particles. The primary difference between the two conditions is the increased amount of internally mixed material in the 13,000 RPM setting. It is important to note that although the 13,000 RPM condition contains a significantly higher volatile mass fraction and volatile particle number fraction, this makes very little difference in the total volatile to non-volatile mass ratio. This is because the additional volatile material occurs at smaller particle sizes which contribute very little to the total mass concentration.

3.3 Conclusion

This study presented quantitative, size-segregated measurements of the mixing state of particulate from a Gnome turbine engine. Measurements of the volatile mass fraction and volatile number fraction of the soot at different mobility diameters were combined

with the measured size distribution to construct mass distributions of the non-volatile, internally mixed volatile, and externally mixed volatile components of the particulate. A comprehensive picture of the mixing state of the soot from the 13,000 RPM and 22,000 RPM engine conditions was produced. Both samples were shown to be predominantly non-volatile (82% for the 13,000 RPM condition; 85% for the 22,000 RPM condition, by mass) with a similar amount of externally mixed volatile material (11% and 12%, respectively). The main difference between the two engine conditions was the increased amount of internally mixed volatile material in the 13,000 RPM condition (7% compared to 3% for the 22,000 RPM condition). The size-segregated measurements make it clear that the additional volatile material in the 13,000 RPM condition is concentrated in smaller particles which contribute very little to the total particulate mass. From general similarities between the morphology and effective densities of the Gnome engine soot that we measured, and those of soot from other aircraft engines, we may suspect that similar trends in the mixing state exist in other engines. Finally, similar trends have also been observed in samples from a miniCAST soot generator (Chapter 2).

3.4 Bibliography

- Abegglen, M., Durdina, L., Brem, B., Wang, J., Rindlisbacher, T., Corbin, J., et. al. (2015). Effective density and mass–mobility exponents of particulate matter in aircraft turbine exhaust: Dependence on engine thrust and particle size. *Journal of Aerosol Science*, 88, 135-147.
- China, S., Mazzoleni, C., Gorkowski, K., Aiken, A. C., & Dubey, M. K. (2013). Morphology and mixing state of individual freshly emitted wildfire carbonaceous particles. *Nature Communications*, 4, 2122. <http://doi.org/10.1038/ncomms3122>
- China, S., Scarnato, B., Owen, R. C., Zhang, B., Ampadu, M. T., Kumar, S., ... Mazzoleni, C. (2015). Morphology and mixing state of aged soot particles at a remote marine free troposphere site: Implications for optical properties. *Geophysical Research Letters*, 42(4), 1243–1250. <http://doi.org/10.1002/2014GL062404>
- Cross, E. S., Onasch, T. B., Ahern, A., Wrobel, W., Slowik, J. G., Olfert, J., ... Davidovits, P. (2010). Soot Particle Studies—Instrument Inter-Comparison—Project Overview. *Aerosol Science and Technology*, 44(8), 592–611. Retrieved from <http://dx.doi.org/10.1080/02786826.2010.482113>
- Durdina, L., Brem, B.T., Abegglen, M., Lobo, P., Rindlisbacher, T., & Thomson, K.A., et al. (2014). Determination of PM mass emissions from an aircraft turbine engine using

- particle effective density. *Atmospheric Environment*, 99, 500–507, <http://dx.doi.org/10.1016/j.atmosenv.2014.10.018>
- Ghazi, R., Tjong, H., Soewono, A., Rogak, S. N., and Olfert, J. S. (2013). Mass, mobility, volatility, and morphology of soot particles generated by a McKenna and inverted burner. *Aerosol Science and Technology*, 47(4), 395-405.
- Graves, B., Olfert, J. S., Patychuk, B., Dastanpour, R. & Rogak, S. (2015). Characterization of Particulate Matter Morphology and Volatility from a Compression-Ignition Natural-Gas Direct-Injection Engine. *Aerosol Science & Technology* 49(8), 589-598. <http://doi.org/10.1080/02786826.2015.1050482>
- Johnson, T., Olfert, J., Symonds, J., Johnson, M., Rindlisbacher, T., Swanson, J., et al. (2015). Effective density and mass-mobility exponent of aircraft turbine particulate matter. *Journal of Propulsion and Power*, 31(2), 573-581.
- Lee, A. K. Y., Willis, M. D., Healy, R. M., Onasch, T. B., & Abbatt, J. P. D. (2015). Mixing state of carbonaceous aerosol in an urban environment: single particle characterization using the soot particle aerosol mass spectrometer (SP-AMS). *Atmospheric Chemistry and Physics*, 15(4), 1823–1841. <http://doi.org/10.5194/acp-15-1823-2015>
- Lobo, P., Durdina, L., Smallwood, G., Rindlisbacher, T., Siegerist, F., Black, E., et al. (2015). Measurement of Aircraft Engine Non-Volatile PM Emissions: Results of the Aviation-Particle Regulatory Instrumentation Demonstration Experiment (A-PRIDE) 4 Campaign. *Aerosol Science and Technology*, 49(7), 472-484.
- McMeeking, G. R., Morgan, W. T., Flynn, M., Highwood, E. J., Turnbull, K., Haywood, J., & Coe, H. (2011). Black carbon aerosol mixing state, organic aerosols and aerosol optical properties over the United Kingdom. *Atmospheric Chemistry and Physics*, 11(17), 9037–9052. <http://doi.org/10.5194/acp-11-9037-2011>
- Momenimovahed, A. & Olfert, J. S. (2015). Effective Density and Volatility of Particles Emitted from Gasoline Direct Injection Vehicles and Implications for Particle Mass Measurement. *Aerosol Science & Technology* 49(11), 1051-1062. <http://doi.org/10.1080/02786826.2015.1094181>
- Moteki, N., & Kondo, Y. (2007). Effects of Mixing State on Black Carbon Measurements by Laser-Induced Incandescence. *Aerosol Science and Technology*, 41(4), 398–417. <http://doi.org/10.1080/02786820701199728>
- NIOSH. (2003). Monitoring of Diesel Particulate Exhaust in the Workplace, Chapter Q, Third Supplement to NMAM, in NIOSH Manual of Analytical Methods, 4th ed., P. F. O'Connor, P. C. Schlecht, eds., NIOSH, Cincinnati, OH, USA. NIOSH DHHS Publication No. 2003-154
- Onasch, T. B., Trimborn, A., Fortner, E. C., Jayne, J. T., Kok, G. L., Williams, L. R., ... Worsnop, D. R. (2012). Soot Particle Aerosol Mass Spectrometer: Development, Validation, and

- Initial Application. *Aerosol Science and Technology*, 46(7), 804–817.
<http://doi.org/10.1080/02786826.2012.663948>
- Petzold, A., Fiebig, M., Fritzsche, L., Stein, C., Schumann, U., Wilson, C. W., ... Technology, C. (2005). Particle emissions from aircraft engines – a survey of the European project PartEmis. *Meteorologische Zeitschrift*, 14(4), 465–476. <http://doi.org/10.1127/0941-2948/2005/0054>
- Ristimäki, J., Vaaraslahti, K., Lappi, M., and Keskinen, J. (2007). Hydrocarbon Condensation in Heavy-Duty Diesel Exhaust. *Environ. Sci. Technol.*, 41:6397–6402.
- Sakurai, H., Park, K., McMurry, P. H., Zarling, D. D., Kittleson, D. B., and Ziemann, P. J. (2003). Size-Dependent Mixing Characteristics of Volatile and Nonvolatile Components in Diesel Exhaust Aerosols. *Environ. Sci. Technol.*, 37:5487–5495.
- Schwarz, J. P., Spackman, J. R., Gao, R. S., Perring, A. E., Cross, E., Onasch, T. B., Ahern, A., Wrobel, W., Davidovits, P., Olfert J., Dubey, M. K., Mazzoleni C. & Fahey D. W. (2010). The Detection Efficiency of the Single Particle Soot Photometer. *Aerosol Science and Technology*, 44(8), 612-628. <http://doi.org/10.1080/02786826.2010.481298>
- Wang, Q., Huang, R.-J., Cao, J., Han, Y., Wang, G., Li, G., ... Zhou, Y. (2014). Mixing State of Black Carbon Aerosol in a Heavily Polluted Urban Area of China: Implications for Light Absorption Enhancement. *Aerosol Science and Technology*, 48(7), 689–697.
<http://doi.org/10.1080/02786826.2014.917758>

4. Demonstration of the CPMA-Electrometer System for Calibrating Black Carbon Particulate Mass Instruments¹

4.1 Introduction

The Committee on Aviation Environmental Protection and the International Civil Aviation Organization are developing new standards and adopting recommended practices which will quantify and regulate mass and number concentrations of particulate emissions from aviation gas turbine engines. SAE E-31, the Aircraft Exhaust Emissions Measurement Committee, is currently investigating instruments and sampling methods for particle number and mass measurement. Although the recommended practices are still being developed, it is likely that only non-volatile particle number concentration will be measured with a dilution system, volatile particle remover, and condensation particle counter (SAE, 2013), similar to the Euro 6 emission standard for light-duty automotive emissions in Europe (Commission Regulation (EC) No 459/2012). Given the large expense of aircraft engine testing and relatively low particle mass concentrations emitted from engines, it is impractical to use a gravimetric filter-based method to measure particle mass concentration. Although the particulate matter emitted from engines can be comprised of black carbon, organic carbon, sulphate, and metals (Petzold et al., 1998; Lee et al., 2010), only the black carbon and metals would be considered non-volatile particulate matter. The SAE E-31 committee is currently considering measuring only the black carbon fraction because it can be readily measured in real-time with existing instrumentation. The instruments under consideration by SAE E-31 are the laser-induced incandescence instrument (LII 300) (Snelling et al., 2005) and the photo-acoustic Micro-Soot Sensor (MSS) (Schindler et al., 2004). Both of these instruments use the absorption of light energy by black carbon to determine its mass concentration; the LII measures the resultant incandescence of the particles, while the MSS measures the pressure wave caused by the particles heating the surrounding air, amplified in a resonance chamber. While the signal the

¹ A version of this chapter has been published as Dickau, M., Johnson, T., Thomson, K., Smallwood, G. & Olfert, J. (2015) Demonstration of the CPMA-Electrometer System for Calibrating Black Carbon Particulate Mass Instruments, *Aerosol Science and Technology*, 49(3), 152-158.

instruments measure is proportional to black carbon concentration, the constant of proportionality is not known in practice, either due to the uncertainties in the theoretical models (such as particle composition and morphology) or the instrument construction and operation. Consequently, the LII and MSS instruments require calibration by a traceable system. Currently, calibration of these instruments relies on filter measurements according to the NIOSH 5040 standard. In the NIOSH method, black carbon (or elemental carbon; EC) and any organic carbon (OC) is collected on a filter, which is then subjected to high temperature in a helium environment and the quantity of OC is measured with a flame ionization detector (FID). Then the remaining material (EC) is subjected to an oxygen environment to convert the carbon to carbon dioxide, which is further reduced to methane and measured with the FID (NIOSH, 2003).

Previously, Symonds et al. (2013) have shown that a centrifugal particle mass analyzer, or CPMA (Olfert et al., 2005), can be used in conjunction with an aerosol electrometer to generate and measure the mass concentration of a charged test aerosol in real-time. The CPMA-electrometer system offers significant advantages as a calibration standard over the filter-based NIOSH 5040 method. The CPMA-electrometer system generates and measures the mass concentration directly from traceable quantities. While a set of NIOSH 5040 filter samples can take hours or days to collect, the CPMA-electrometer system can take an entire range of measurements in 10 to 15 minutes. Furthermore, the diluted black carbon mass concentrations measured from the proposed aircraft gas turbine sampling system are relatively low, often below $100 \mu\text{g}/\text{m}^3$. These low concentrations increase the required sampling time and measurement uncertainty of the NIOSH method, compared to the CPMA-electrometer system.

The purpose of this chapter is to demonstrate the feasibility of the CPMA-electrometer system to traceably generate and measure the mass concentration of particulate black carbon for the calibration of two LII and two MSS systems. The effect of electric particle charge, CPMA resolution, and linearity and uncertainty of the system is examined.

4.2 Theory

The centrifugal particle mass analyzer classifies aerosol particles by their mass-to-charge ratio by balancing centrifugal and electrostatic forces between two concentric rotating cylinders (Olfert et al., 2005). An electrically-charged aerosol enters the CPMA, and only particles with a narrow range of mass-to-charge ratio will pass through the instrument. Other particles will impact the walls of the cylindrical classification section and will not pass through the instrument. Furthermore, low-mass uncharged particles may fail to be removed by the centrifugal forces, and so may also pass through. The selected mass-to-charge ratio is controlled by setting the voltage potential difference (V) and rotational speed of the CPMA cylinders (where the inner cylinder is spun slightly faster than the outer cylinder to improve the penetration efficiency). In practice the CPMA software selects the appropriate voltage and rotational speed based on the desired mass-to-charge ratio and resolution. It can be shown that the particle mass (m) per unit charge (q), or the specific mass (s) is given by,

$$s = \frac{m}{q} = \frac{V}{\omega^2 r_c^2 \ln(r_2/r_1)} \quad (4.1)$$

where r_1 and r_2 are the radii of the CPMA inner and outer cylinders, r_c is the mean radius, and ω is the rotational speed of the gas at the mean radius (Olfert et al., 2005). After classification, the mass concentration of the aerosol, $M_{\text{classified}}$, can be expressed as,

$$M_{\text{classified}} = M_0 + s(1eN_{+1} + 2eN_{+2} + 3eN_{+3} + \dots) \quad (4.2)$$

where M_0 is the mass concentration of uncharged particles which escape classification, e is the electronic charge (1.6×10^{-19} C), and N_{+i} are the number concentrations of particles with i positive charges (Symonds et al., 2013).

Once classified by the CPMA, the aerosol sample is pulled through a Faraday cup aerosol electrometer using a vacuum pump. The aerosol electrometer measures the electrical current of the flow of charged aerosol particles by passing the sample through a HEPA filter, capturing the aerosol particles inside of an enclosed metal cylinder acting as a Faraday cage. The charge that is built up inside the cylinder is balanced by an

equal charge drawn to the cylinder, which is measured. The Faraday cup is isolated from any other electrical contact by insulating Teflon rings between contact surfaces, and by placing the entire system inside another Faraday cage. Measuring the sample flow rate through the aerosol electrometer, the current will be,

$$I = Q(1eN_{+1} + 2eN_{+2} + 3eN_{+3} + \dots) \quad (4.3)$$

where Q is the volume flow rate of the aerosol.

The mass concentration of uncharged particles that pass through the CPMA can be mitigated by highly charging the aerosol with a unipolar charger, and by increasing the centrifugal forces by increasing the rotational speed of the CPMA. Assuming M_0 is negligible, the mass concentration can be found in terms of the following measured quantities,

$$M_{\text{classified}} = \frac{sI}{Q} \quad (4.4)$$

As a classifier, the CPMA selects a narrow range of specific masses, centered on s . The resolution, R_{CPMA} , of the CPMA characterises the width of this range. The resolution is the specific mass setpoint divided by the full-width-half-maximum range of the CPMA transfer function, where the transfer function is the probability that a particle of a given specific mass is transferred through the CPMA. The resolution may be increased (range of classified specific masses made narrower) by increasing the rotational speed.² The derivation of Equation 4.4 assumes that the particle mass distribution of the classified aerosol above and below s are balanced (i.e. there is an equal mass concentration of particles greater and less than s exiting the CPMA, which will depend on the distribution of particles entering the CPMA); an assumption that grows more accurate as the resolution increases. Further explanation on the bias uncertainty created by this assumption is shown in the supplementary information of Symonds et al. (2013).

² More information about determining resolution can be found in Tajima et al. (2011), which discusses the resolution of the aerosol particle mass analyser (APM). The APM operates very similarly to the CPMA, and the way that the resolution is defined and determined is directly comparable.

4.3 Experimental Setup

The experimental setup is shown in Figure 4.1. Soot was generated by a co-flow inverted diffusion-flame burner using methane as a fuel (Stipe et al., 2005). The combustion flow rates were 1.4 L/min methane with 16.6 L/min dry air (all flow rates are stated at standard conditions; 0 °C, 101.325 kPa). 85 L/min of dilution air (at standard conditions) was added to the exhaust gas to prevent water or other volatile material from condensing on the soot particles. A sample line of 4 L/min was drawn from the diluted exhaust and passed through a cyclone to remove large particles ($d_p > 1 \mu\text{m}$). The aerosol was drawn continuously through the system with a vacuum pump, and the flow rates were controlled and measured using Aalborg GFC mass flow controllers. Particle mobility-size distributions, measured using a scanning mobility particle sizer (SMPS, TSI Inc), revealed the aerosol had a median mobility diameter of 199 nm and a geometric standard deviation of 1.83 after passing through the cyclone and the conditioning system.

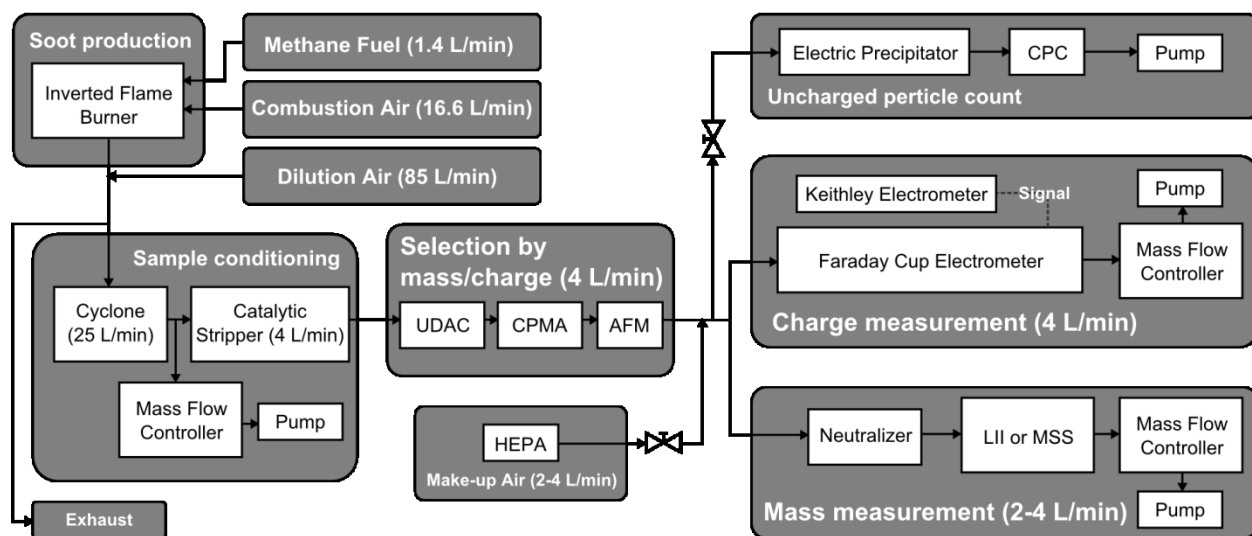


Figure 4.1: Diagram of experimental setup.

Because the CPMA-electrometer system measures total particulate mass, while the LII and MSS only measure the non-volatile black carbon component, the soot was conditioned by passing it through a catalytic converter heated to 350°C to remove the volatile species. NIOSH 5040 analysis showed that the ratio of the EC to total carbon was on average 98.8% with a standard deviation of 0.8% on three tests. Based on this,

the results of the experiment were calculated assuming that no volatile component was present, and that the two systems were measuring the same quantity (i.e. all particulate was black carbon). In principle, the CPMA-electrometer system could be used with any aerosol source, including other combustion sources (e.g. miniCAST or diesel, gasoline, or gas turbine engines) or atomized suspensions of graphite (e.g. Aquadag®) or 'fullerene soot' (e.g. Alfa Aesar stock # 40971). However, as shown by Maricq (2014), the non-volatile component of some soot sources may contain a significant fraction of mass that is not black carbon (i.e. non-volatile organic compounds or fullerene).

The conditioned sample was charged using a unipolar diffusion aerosol charger (UDAC, Cambustion Ltd.) (Biskos et al., 2005), placing a high net-positive charge on the soot particles (several elementary charges per particle). The charger was operated with an n/t product of approximately 4×10^{13} s/m³ and a sample flow rate of 4 L/min. The CPMA-electrometer mass concentration measurement is independent of the charge state of the aerosol, but this high-charge state increases the measured current and reduces the number of uncharged particles. The charged sample was then classified by the CPMA at a set mass-to-charge ratio, with the CPMA also operating at a sample rate of 4 L/min. An aerosol flow meter (AFM; Cambustion Ltd.) measured the flow rate of the sample exiting the CPMA. Each data point in the experiment represents a measurement of the classified mass concentration at a set mass-to-charge ratio and resolution; mass-to-charge ratios in the range of 0.1 to 1 fg per elementary charge were used, corresponding to a range of particle sizes roughly centered around the median size of the source aerosol. The resolution used was either 4.5 or 6.5. This resulted in rotational speeds and voltages in the range of 750 to 1250 rad/s and 50 to 150 V, respectively.

Occasional checks were performed to determine if any uncharged particles were passing through the CPMA, using an electric precipitator and a condensation particle counter (CPC, TSI Inc) following classification. As shown by Symonds et al. (2013), the majority of uncharged particles that can be classified by the CPMA with a UDAC are below 12 nm in diameter under typical operating conditions. Most of these particles were lost by diffusion in the catalytic stripper or in the long sampling line (~5 m) between the catalytic stripper and the UDAC, hence, even under low rotational speed in the

CPMA, the uncharged particle number concentration was found to be zero or only a few particles per cubic centimeter (with an equivalent mass concentration orders of magnitude lower than the measured mass concentration).

After classification, 2 to 4 L/min of HEPA filtered make-up air was added to the sample flow to have sufficient flow rate for both measurement instruments. Then the sample was split between the aerosol electrometer (4 LPM) and the challenge instrument (2 L/min for the LII 300, or 4 L/min for the MSS), allowing both instruments to measure the same mass concentration. The current drawn to the aerosol electrometer was measured by a Keithley 6514 electrometer. The mass concentration was varied by changing the CPMA setpoint, s , allowing a different fraction of the sample through. At each setpoint, the measured mass concentration was averaged over 40 seconds before adjusting the CPMA to the next point. Typically 10 setpoints were chosen across the desired range, allowing the CPMA-electrometer system to generate 10 data points for calibrating the challenge instrument in approximately 10 to 15 minutes. Two LII 300 instruments (serial numbers 0343 and 0340) and two MSS instruments (serial numbers 1187 and 0273) were used to compare against the CPMA-electrometer system. The LII and MSS instruments were calibrated using NIOSH 5040 within two months of these experiments. The mass concentrations reported herein, and used in the comparison, include this calibration.

In some of the tests, the part of the sample entering the challenge instrument was first passed through a radioactive charge neutralizer (Kr-85), which neutralized the high unipolar charge state on the aerosol and replaced it with a lower bipolar equilibrium charge state. Measurements with and without the neutralizer were compared to see if the high charge state used in the CPMA affects the measurements of the LII or MSS. Measurements were also performed with the CPMA set at different resolutions to determine if that has any significant influence on the measurement system.

4.4 Results and Discussion

4.4.1 Linearity and Uncertainty

Comparisons of the measurements of the CPMA-electrometer system and those of the two LII and two MSS instruments are shown in Figure 4.2. The instruments were compared for the base case of using the neutralizer before the challenge instrument, and operating the CPMA at the high resolution of $R_{CPMA}=6.5$. For both types of challenge instruments, the mass concentration was varied from about $5 \mu\text{g}/\text{m}^3$ to over $100 \mu\text{g}/\text{m}^3$.

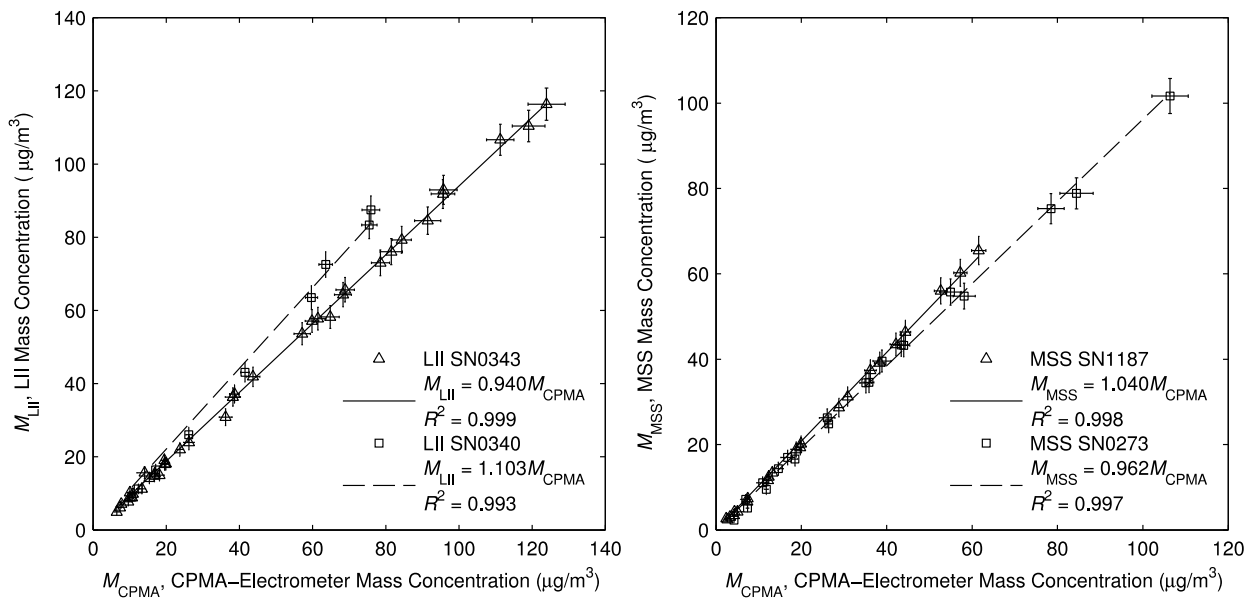


Figure 4.2: Comparison of soot mass concentration measurements by the CPMA-electrometer system to those by (a) two LII 300 instruments and (b) two MSS instruments, all measurements with a neutralizer and with the CPMA set at resolution of approximately $R_{CPMA} = 6.5$.

Considering the lines of best fit shown in Figure 4.2, the LII models had slopes of 0.940 and 1.103, and R^2 values of 0.999 and 0.993 respectively. The MSS models had slopes of 1.040 and 0.962, with R^2 values of 0.998 and 0.997. All instruments showed highly linear correlations between the instruments across the entire measurement range. The fact that all the data is highly linear means that the CPMA-electrometer and LII/MSS instruments must be highly linear. As mentioned in the Experimental Setup, the LII and MSS instruments were calibrated to NIOSH 5040 and there was good agreement between the CPMA-electrometer measurements and the instruments calibrated by

NIOSH 5040 (i.e. slopes are close to unity). However, the purpose of these measurements is not to compare the accuracy of the instruments (or slopes of the fit) because of the possibility systematic error in the NIOSH 5040 or CPMA-electrometer calibrations or because of drift in the LII or MSS instruments between calibrations. Rather, the experiments are intended to investigate the feasibility of the CPMA-electrometer system as a calibration method. Therefore, the linearity of the experimental results is of more interest than the slopes. The uncertainty in the CPMA-electrometer method is better understood by examining the sources of error in the system, which is done presently.

The measurement uncertainty of the CPMA-electrometer system is compared to the amount of variation expected from using the NIOSH method. The standard uncertainty (coverage factor, $k=1$) in the CPMA-electrometer measurements is shown as horizontal error bars in the figures. The relative standard uncertainty averaged 4.3% and was as low as 2.6% for some measurements. The uncertainty in the CPMA-electrometer measurements had four main sources, which were combined using the soot sum of the squares to find the total standard uncertainty. The flow meter controlling the flow rate had a stated uncertainty of 1.5%, which was converted to a standard uncertainty for the calculation. The uncertainty in the CPMA set point, calculated from the voltage, rotational speed, and radii of the cylinders, was approximately 1.4% as shown by Symonds et al. (2013). There is a small amount of bias error that arises due to the finite resolution of the CPMA. Calculations following the method described in the supplementary material in Symonds et al. (2013) for a resolution of $R_{\text{CPMA}} = 6.5$, estimate that this error is no greater than 1%. To be conservative, an uncertainty of 1.5% was factored in to account for this unknown error.

The remainder of the uncertainty came from the measurement of the current, with a precision uncertainty component from the accuracy of the electrometer and from the fluctuations of the current (together around 1% to 1.5%), and a bias uncertainty component from a zero offset drift in the aerosol electrometer. The zero offset was measured before and after each test while the sample line was filtered with the HEPA filter to ensure no particles; the offset used in calculating the results was the average of

before and after the measurements. Typical values of the zero offset were 0.1 to 1 pA, compared to measured currents of 1 to 10 pA, with a drift of 0.2 to 0.5 pA. The uncertainty caused by the drifting zero offset alone was often around 3%, and in extreme cases (low concentrations) it was the single largest source of uncertainty in the CPMA-electrometer measurement. Since these experiments were conducted, improvements to a similar Faraday cup electrometer (using higher purity Teflon for the electrical insulation) have proved successful in reducing the offset to around 50 fA, with 10 to 20 fA drift. Thus, for future experiments, we expect the uncertainty from the electrometer measurement to be much lower, leading to total standard uncertainties for the CPMA-electrometer system of approximately 3% or less.

Below 100 $\mu\text{g}/\text{m}^3$, the uncertainty of the CPMA-electrometer system compares favorably to the NIOSH 5040 calibration method. NIOSH (2003) states the NIOSH 5040 method has a relative standard deviation of 8.5% at 23 $\mu\text{g}/\text{m}^3$. The standard deviation of the NIOSH method is shown as vertical error bars in the figures. These uncertainties were estimated from the stated value at 23 $\mu\text{g}/\text{m}^3$, and the observation that “[t]he variance [square of the standard deviation] was roughly proportional to the mean concentration; therefore, the relative standard deviation (RSD) decreased with increasing concentration” (NIOSH, 2003). Assuming this relationship holds,

$$\sigma_{\text{NIOSH}} = (0.085 \cdot 23 \mu\text{g}/\text{m}^3) \cdot \left(\frac{M_{\text{NIOSH}}}{23 \mu\text{g}/\text{m}^3} \right)^{1/2} \quad (4.5)$$

$$RSD_{\text{NIOSH}} = \frac{\sigma_{\text{NIOSH}}}{M_{\text{NIOSH}}} = 0.085 \cdot \left(\frac{23 \mu\text{g}/\text{m}^3}{M_{\text{NIOSH}}} \right)^{1/2} .$$

It is important to note that the NIOSH 5040 relative standard deviation represents a lower bound on the total uncertainty of the NIOSH 5040 method as it only accounts for variability between measurements and does not include any bias uncertainties. The actual uncertainty of the NIOSH 5040 method must be greater than RSD_{NIOSH} . Nevertheless, the relative standard deviation of the NIOSH 5040 method decreases to become comparable to the total uncertainty of the CPMA-electrometer system above mass concentrations of 100 $\mu\text{g}/\text{m}^3$. At low particle concentrations, the CPMA system has lower uncertainty than the NIOSH method. At the higher end of the range of

concentrations examined, the uncertainty in the CPMA-electrometer system is similar to the RSD of the NIOSH method.

4.4.2 Effect of Charge Neutralizer

One concern about using the CPMA-electrometer system as a calibration standard for the LII and MSS instruments was that the high electrical charge state of the particles exiting the CPMA might affect the measurements of the challenge instruments in some way. Results with and without a radioactive charge neutralizer (Kr-85) installed before the challenge instruments are compared in Figure 4.3. The residuals of both the neutralized and non-neutralized sets of data, referenced to the regression line for the base case, were of similar magnitude and were comparable to the experimental uncertainty. This agrees with visual examination of the results, which suggests that the effect of the neutralizer was not significant.

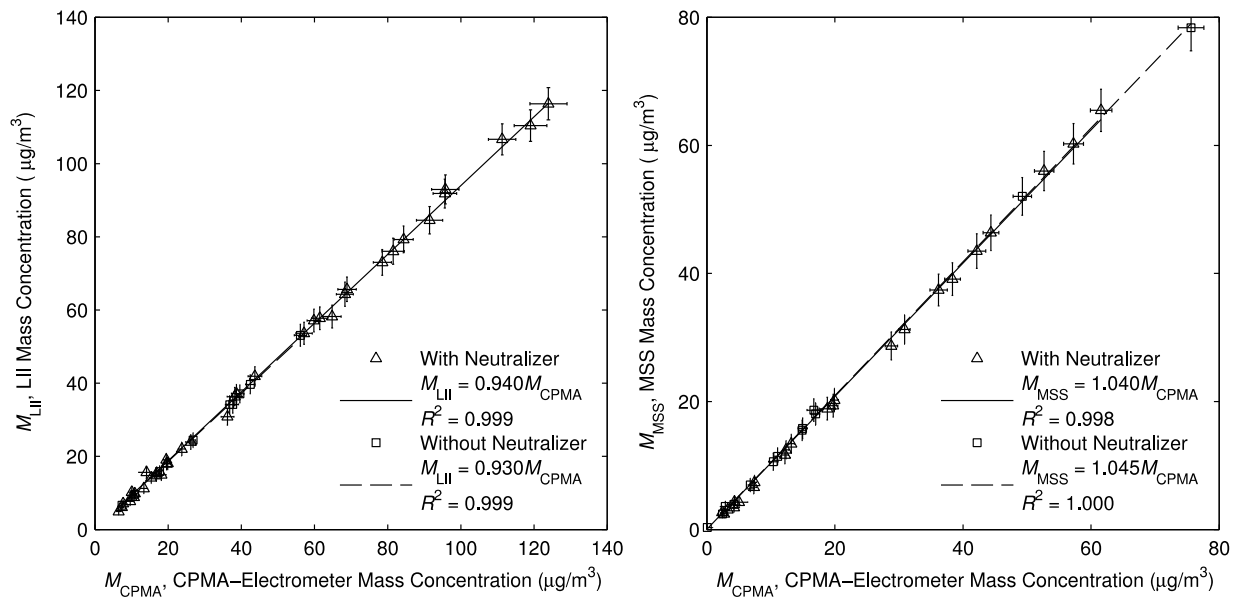


Figure 4.3: Mass concentration measurements with and without a neutralizer for (a) the LII 300 SN0343 and (b) the MSS SN1187, all measurements with the CPMA set at resolution of approximately $R_{CPMA} = 6.5$.

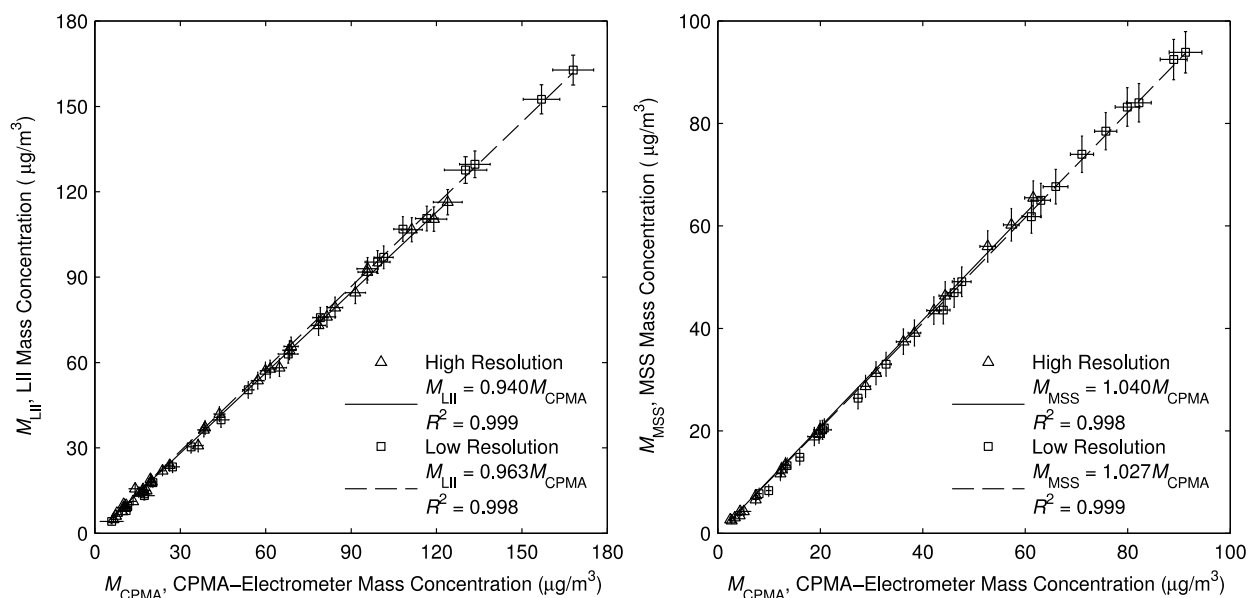


Figure 4.4: Mass concentration measurements with the CPMA set at resolutions of approximately $R_{CPMA} = 4.5$ and $R_{CPMA} = 6.5$ for (a) the LII 300 SN0343 and (b) the MSS SN1187, both with a neutralizer.

4.4.3 Effect of CPMA Resolution

One further question to resolve was whether the resolution of the CPMA had any effect on the measurements of the CPMA-electrometer system. Specifically, this effect would be due to the bias error introduced by assuming that the masses of particles in the narrow classification band balance out above and below the setpoint. A higher resolution produces a smaller error, but allows fewer particles through and therefore lowers the measured concentration. Figure 4.4 compares results where the CPMA resolution was set to a value of approximately 4.5, with those where the resolution was set to approximately 6.5.³ Comparison of the residuals of the high-resolution and low-resolution data sets, alongside visual examination, again showed that there is little difference between the two. This agrees with our expectation, based on calculations of the error introduced by the finite CPMA resolution, which estimate that the error is small for the two cases. These calculations were done according to the method described in the supplementary material of Symonds et al. (2013), and estimated typical bias errors no greater than 0.5% for the high resolution case, and 1% for the low resolution case.

³ The CPMA controls the resolution assuming the particles have a constant effective density; however, because the effective density of fractal-like aggregate particles like soot is dependent on their size, the actual resolution varies slightly over the different mass setpoints used in the test.

4.5 Conclusions

Previous experiments have shown the viability of the CPMA-electrometer system for measuring the mass concentration of a silicone oil test aerosol. The results of the described experiments now demonstrate the viability of the CPMA-electrometer system as a fast, traceable mass measurement system well suited for nanoparticulate black carbon. Compared to methods using filter sampling, such as gravimetric or EC/OC measurements, this system can generate data points in minutes rather than hours, and it is not susceptible to filter sampling artifacts. These characteristics make it suitable as a calibration method for less traceable instruments such as the LII or MSS.

The system has a relatively low standard uncertainty, averaging 4.3% in these experiments. A major source of uncertainty was in the measurement of the current by the aerosol electrometer, which suffered from a drifting zero offset. With improvements to the electrometer and the diffusion charger to reduce these performance issues, the uncertainty in the system could be made as low as 2.5% to 3%. The low uncertainty of the CPMA-electrometer system at low particle concentrations, the close agreement of its measurements to those of the NIOSH 5040 calibrated LII 300 and MSS, and the highly linear correlation between them, are all indications of its suitability as a calibration method. Furthermore, highly charged particles exiting the CPMA did not significantly influence the LII or MSS measurements thus the charge neutralizer is not required in future calibrations.

4.6 Bibliography

- Biskos, G., Reavell, K., Collings, N. (2005). Unipolar diffusion charging of aerosol particles in the transition regime. *Journal of Aerosol Science*. 36:247-265.
- Ghazi, R., Tjong, H., Soewono, A., Rogak, S., Olfert, J. (2013). Mass, mobility, volatility, and morphology of soot particles generated by a McKenna and inverted burner. *Aerosol Science and Technology*. 47:395-405.
- ICAO. (2008). ICAO Annex 16: Environmental Protection, Volume II – Aircraft Engine Emissions. *International Civil Aviation Organization*, Montreal, Canada.
- Lee, D. S., Pitari, G., Grewe, V., Gierens, K., Penner, J. E., Petzold, A., Prather, M. J., Schaumann, U., Bais, A., Berntsen, T., Iachetti, D., Lim, L. L., Sausen, R. (2010).

- Transport impacts on atmosphere and climate: Aviation. *Atmospheric Environment*. 44(37):4678-4734.
- Maricq, M. M. (2014). Examining the Relationship between Black Carbon and Soot in Flames and Engine Exhaust. *Aerosol Science and Technology*. 48:620-629.
- NIOSH. (2003). O'Connor, Schlecht, in: NIOSH Manual of Analytical Methods. Monitoring of Diesel Particulate Exhaust in the Workplace, Chapter Q, Third Supplement to NMAM, 4th Edition, NIOSH DHHS Publication No. 2003-154.
- Official Journal of the European Union (2012). Commission Regulation (EC) No 459/2012.
- Olfert, J., Collings, N. (2005). New method for particle mass classification – the Couette centrifugal particle mass analyzer. *Journal of Aerosol Science*. 36:1338-1352.
- Petzold, A., Ström, J., Ohlsson, S., Schröder, F. P. (1998). Elemental composition and morphology of ice-crystal residual particles in cirrus clouds and contrails. *Atmospheric Research*. 49(1):21-34.
- SAE. (2011). SAE Aerospace Recommended Practice 1179 Rev D, "Aircraft Gas Turbine Engine Exhaust Smoke Measurement", *SAE International*.
- SAE. (2013). SAE Aerospace Information Report 6241, "Procedure for the Continuous Sampling and Measurement of Non-Volatile Particle Emissions from Aircraft Turbine Engines", *SAE International*.
- Schindler, W., Haisch, C., Beck, H., Niessner, R., Jacob, E., Rothe, D. (2004). A Photoacoustic Sensor System for Time Resolved Quantification of Diesel Soot Emissions. *SAE Technical Papers*.
- Snelling, D., Smallwood, G., Liu, F., Gülder, Ö., Bachalo, W. (2005). A calibration-independent laser-induced incandescence technique for soot measurement by detecting absolute light intensity. *Applied Optics*. 44:6773-6785.
- Stipe, C., Higgins, B., Lucasa, D., Koshland, C., Sawyer, R. (2005). Inverted Co-Flow Diffusion Flame for Producing Soot. *Review of Scientific Instruments*. 76:23–908.
- Symonds, J., Reavell, K., Olfert, J. (2013). The CPMA-Electrometer System – A Suspended Particle Mass Concentration Standard. *Aerosol Science and Technology*. 47(8):i-iv.
- Tajima, N., Fukushima, N., Ehara, K., Sakurai, H. (2011). Mass Range and Optimized Operation of the Aerosol Particle Mass Analyzer. *Aerosol Science and Technology*. 45(2):196-214.

5. Conclusion

5.1 Summary and Conclusions

This research has focused on advancing our ability to study and characterize particulate emissions from aircraft gas turbine engines, through two paths. First, because aircraft particulate emissions are often comprised of a mix of non-volatile and volatile material, and because the mixing state significantly affects properties of the particulate matter, a way to measure and characterize the mixing state is necessary. In Chapter 2, a methodology for quantifying the mixing state of an aerosol was described and demonstrated, and in Chapter 3, the mixing state of soot from a typical aircraft gas turbine engine was measured. Second, because calibration is required for the LII 300 and the MSS instruments, which are likely to be used to measure the mass concentration of non-volatile particulate emissions in industry, a traceable mass concentration measurement system needs to be developed and demonstrated. In Chapter 4, the CPMA-electrometer system was demonstrated as a viable calibration method. Combining these two paths of research, by measuring both the mixing state and the non-volatile mass concentration of particulate emissions, a more complete picture of the emitted amounts of both non-volatile and volatile material, as well as the way they are mixed, can be developed.

The methodology described in Chapter 2 was demonstrated to be successful in quantifying different proportions of volatile and non-volatile material, and different levels of internal and external mixing. One of the key limitations of the technique was seen, which was that the density of the independent volatile particles could not be determined due to their low concentration. This is likely to be a common scenario since typical gas turbine engines do not produce high quantities of volatile material. To construct the mass distributions, the volatile material was assumed to have a density equal to that of water, but this is only an order of magnitude estimate. More accurate estimates of the density could be made by chemical analysis of the volatile material.

Mixing states were found to be relatively similar between the diffusion flame soot, generated by a miniCAST and measured in Chapter 2, and the aircraft gas turbine soot, exhausted from a Gnome engine and measured in Chapter 3. The miniCAST high EC setting was comparable to the Gnome high RPM condition, and the miniCAST high OC setting was comparable to the Gnome low RPM condition. Both studies found a moderate quantity of externally mixed volatile material in both the “high EC” and “high OC” conditions, with a low or negligible amount of internally mixed volatile material in the “high EC” condition, and a moderate amount of internally mixed volatile material in the “high OC” condition. Both studies also show that the volatile material, both externally and internally mixed, was generally concentrated in smaller particles, with larger particles being predominantly non-volatile.

Finally, the CPMA-electrometer system was shown in Chapter 4 to successfully measure the mass concentration of soot from an inverted burner, with close agreement and highly linear correlation to the measurements of the LII 300 and MSS. Because the CPMA-electrometer system measures mass traceably, and with relatively low uncertainty, it is suitable as a calibration method for mass concentration measurement instruments. Its speed and lack of reliance on filter papers (which are susceptible to sampling artifacts) are advantages over the current calibration methods.

5.2 Future Work

These two paths of research can, of course, be continued. For quantifying aerosol mixing states, the uncertainty and precision of the methodology can be better delineated, with further experiments and greater amounts of data. The capabilities of the methodology can be explored by measuring different kinds of aerosols. Current instrumentation prevents the resolution of this method from being improved very much, however. The main focus of research in the near future will be on using the CPMA-electrometer system as a calibration method. One of the next steps in this direction is to determine the repeatability of the instruments in the CPMA-electrometer system and the reproducibility between different CPMA-electrometer systems. This can be done in a piece-wise fashion, where the repeatability and reproducibility of each instrument (CPMA, flowmeter, electrometer, etc.) is examined in turn to carefully determine its

contribution to the uncertainty. Ultimately it is hoped that, by improving our ability to measure the mass concentration and the mixing state of aircraft particulate emissions, our understanding of emissions will be furthered, more effective standards and regulations will be adopted, and harmful particulate emissions will be reduced.

Complete Bibliography

- Abegglen, M., Durdina, L., Brem, B., Wang, J., Rindlisbacher, T., Corbin, J., et. al. (2015). Effective density and mass–mobility exponents of particulate matter in aircraft turbine exhaust: Dependence on engine thrust and particle size. *Journal of Aerosol Science*, 88, 135-147.
- Barrett, Steven R. H., Britter, Rex E., Waitz, Ian A. (2010). Global Mortality Attributable to Aircraft Cruise Emissions, *Environmental Science and Technology*. 44 (19):7736–7742.
- Biskos, G., Reavell, K., Collings, N. (2005). Unipolar diffusion charging of aerosol particles in the transition regime. *Journal of Aerosol Science*. 36:247-265.
- Boies, A., Stettler, M., Swanson, J., Johnson, T., Olfert, J., Johnson, M., ... Rogak, S. (2015). Particle Emissions Characteristics of a Gas Turbine with a Double Annular Combustor. *Aerosol Science and Technology*, 49(9), 842-855. doi: 10.1080/02786826.2015.1078452
- Bond, T. C., Doherty, S. J., Fahey, D. W., Forster, P. M., Berntsen, T., DeAngelo, B. J., ... Zender, C. S. (2013). Bounding the role of black carbon in the climate system: A scientific assessment. *Journal of Geophysical Research: Atmospheres*, 118(11), 5380–5552. <http://doi.org/10.1002/jgrd.50171>
- Burnett, R. T., Pope, C. Arden, I., Ezzati, M., Olives, C., Lim, S. S., Mehta, S., ... Cohen, A. (2014). An Integrated Risk Function for Estimating the Global Burden of Disease Attributable to Ambient Fine Particulate Matter Exposure. *Environmental Health Perspectives*.
- Boucher, O., Randall, D., Artaxo, P., Bretherton, C., Feingold, G., & Forster, P., et al (2013). Clouds and aerosols. In T. F. Stocker, D. Qin, G.-K. Plattner, M. Tignor, S. K. Allen, J. Boschung, A. Nauels, Y. Xia, V. Bex, & P. M. Midgley (Eds.), *Climate Change 2013: The physical science basis. Contribution of Working Group I to the Fifth Assessment Report of the Intergovernmental Panel on Climate Change. Cambridge University Press: Cambridge, UK; New York, NY, USA*
- Cappa, C. D., Onasch, T. B., Massoli, P., Worsnop, D. R., Bates, T. S., Cross, E. S., ... Zaveri, R. A. (2012). Radiative absorption enhancements due to the mixing state of atmospheric black carbon. *Science* (New York, N.Y.), 337(6098), 1078–81. <http://doi.org/10.1126/science.1223447>
- Chan, T. W., Brook, J. R., Smallwood, G. J., & Lu, G. (2011). Time-resolved measurements of black carbon light absorption enhancement in urban and near-urban locations of southern Ontario, Canada. *Atmospheric Chemistry and Physics*, 11(20), 10407–10432. <http://doi.org/10.5194/acp-11-10407-2011>

- China, S., Mazzoleni, C., Gorkowski, K., Aiken, A. C., & Dubey, M. K. (2013). Morphology and mixing state of individual freshly emitted wildfire carbonaceous particles. *Nature Communications*, 4, 2122. <http://doi.org/10.1038/ncomms3122>
- China, S., Scarnato, B., Owen, R. C., Zhang, B., Ampadu, M. T., Kumar, S., ... Mazzoleni, C. (2015). Morphology and mixing state of aged soot particles at a remote marine free troposphere site: Implications for optical properties. *Geophysical Research Letters*, 42(4), 1243–1250. <http://doi.org/10.1002/2014GL062404>
- Cross, E. S., Onasch, T. B., Ahern, A., Wrobel, W., Slowik, J. G., Olfert, J., ... Davidovits, P. (2010). Soot Particle Studies—Instrument Inter-Comparison—Project Overview. *Aerosol Science and Technology*, 44(8), 592–611. Retrieved from <http://dx.doi.org/10.1080/02786826.2010.482113>
- Durdina, L., Brem, B.T., Abegglen, M., Lobo, P., Rindlisbacher, T., & Thomson, K.A., et al. (2014). Determination of PM mass emissions from an aircraft turbine engine using particle effective density. *Atmospheric Environment*, 99, 500–507, <http://dx.doi.org/10.1016/j.atmosenv.2014.10.018>
- Ehara, K., Hagwood, C., and Coakley, K. J. (1996). Novel Method to Classify Aerosol Particles According to Their Mass-to-Charge Ratio - Aerosol Particle Mass Analyser. *J. Aerosol Sci.*, 27:217–234.
- Ghazi, R., & Olfert, J. S. (2013). Coating Mass Dependence of Soot Aggregate Restructuring due to Coatings of Oleic Acid and Dioctyl Sebacate. *Aerosol Science and Technology* 47(2), 192-200. <http://doi.org/10.1080/02786826.2012.741273>
- Ghazi, R., Tjong, H., Soewono, A., Rogak, S. N., and Olfert, J. S. (2013). Mass, mobility, volatility, and morphology of soot particles generated by a mckenna and inverted burner. *Aerosol Science and Technology*, 47(4), 395-405.
- Graves, B., Olfert, J. S., Patychuk, B., Dastanpour, R. & Rogak, S. (2015). Characterization of Particulate Matter Morphology and Volatility from a Compression-Ignition Natural-Gas Direct-Injection Engine. *Aerosol Science & Technology* 49(8), 589-598. <http://doi.org/10.1080/02786826.2015.1050482>
- Graves, B. (2015). Characterization of Particulate Matter Morphology and Volatility for Two Direct-Injection Engines. MSc. thesis, *Univeristy of Alberta*.
- ICAO. (2008). ICAO Annex 16: Environmental Protection, Volume II – Aircraft Engine Emissions. *International Civil Aviation Organization*, Montreal, Canada.
- ICAO. (2013). International Civil Aviation Organization. (2013) ICAO 2013 Environmental Report. *International Civil Aviation Organization*, Montreal, Canada. Accessed online at http://cfapp.icao.int/Environmental-Report-2013/files/assets/common/downloads/ICAO_2013_Environmental_Report.pdf

- Jayne, J. T., Leard, D. C., Zhang, X., Davidovits, P., Smith, K. A., Kolb, C. E., & Worsnop, D. R. (2000). Development of an Aerosol Mass Spectrometer for Size and Composition Analysis of Submicron Particles. *Aerosol Science and Technology*, 33(1-2), 49–70. <http://doi.org/10.1080/027868200410840>
- Johnson, T., Olfert, J., Symonds, J., Johnson, M., Rindlisbacher, T., Swanson, J., et al. (2015). Effective density and mass-mobility exponent of aircraft turbine particulate matter. *Journal of Propulsion and Power*, 31(2), 573-581.
- Kinney, P. D., Pui, D. Y. H., Mulholland, G. W., and Bryner, N. P. (1991). Use of the Electrical Classification Method to Size 0.1 μ m SRM Particles—A Feasibility Study. *J. Res. Natl. Inst. Stan. Technol.*, 96:147–176.
- Knutson, E. O. and Whitby, K. T. (1975). Aerosol Classification by Electric Mobility: Apparatus, Theory, and Application, *J. Aerosol Sci.* 6:443–451
- Kuwata, M., Kondo, Y., & Takegawa, N. (2009). Critical condensed mass for activation of black carbon as cloud condensation nuclei in Tokyo. *Journal of Geophysical Research*, 114(D20), D20202. <http://doi.org/10.1029/2009JD012086>
- Lee, A. K. Y., Willis, M. D., Healy, R. M., Onasch, T. B., & Abbatt, J. P. D. (2015). Mixing state of carbonaceous aerosol in an urban environment: single particle characterization using the soot particle aerosol mass spectrometer (SP-AMS). *Atmospheric Chemistry and Physics*, 15(4), 1823–1841. <http://doi.org/10.5194/acp-15-1823-2015>
- Lee, D. S., Pitari, G., Grewe, V., Gierens, K., Penner, J. E., Petzold, A., Prather, M. J., Schaumann, U., Bais, A., Berntsen, T., Iachetti, D., Lim, L. L., Sausen, R. (2010). Transport impacts on atmosphere and climate: Aviation. *Atmospheric Environment*. 44(37):4678-4734.
- Lighty, J. S., Veranth, J. M., & Sarofim, A. F. (2000). Combustion aerosols: Factors governing their size and composition and implications to human health. *Journal of the Air & Waste Management Association*, 50(9), 1565–1618, <http://dx.doi.org/10.1080/10473289.2000.10464197>.
- Liu, D., Allan, J., Whitehead, J., Young, D., Flynn, M., Coe, H., ... Bandy, B. (2013). Ambient black carbon particle hygroscopic properties controlled by mixing state and composition. *Atmospheric Chemistry and Physics*, 13(4), 2015–2029. <http://doi.org/10.5194/acp-13-2015-2013>
- Lobo, P., Durdina, L., Smallwood, G., Rindlisbacher, T., Siegerist, F., Black, E., et al. (2015). Measurement of Aircraft Engine Non-Volatile PM Emissions: Results of the Aviation-Particle Regulatory Instrumentation Demonstration Experiment (A-PRIDE) 4 Campaign. *Aerosol Science and Technology*, 49(7), 472-484.

- Mamakos, A., Khalek, I., Giannelli, R. & Spears, M. (2013). Characterization of Combustion Aerosol Produced by a Mini-CAST and Treated in a Catalytic Stripper. *Aerosol Science & Technology* 47(8), 927-936. doi: 10.1080/02786826.2013.802762
- Maricq, M. M. (2007). Coagulation dynamics of fractal-like soot aggregates. *Journal of Aerosol Science*, 38(2), 141–156, <http://dx.doi.org/10.1016/j.jaerosci.2006.11.004>.
- McFiggans, G., Artaxo, P., Baltensperger, U., Coe, H., Facchini, M. C., Feingold, G., ... Weingartner, E. (2006). The effect of physical and chemical aerosol properties on warm cloud droplet activation. *Atmospheric Chemistry and Physics*, 6(9), 2593–2649. <http://doi.org/10.5194/acp-6-2593-2006>
- McMeeking, G. R., Morgan, W. T., Flynn, M., Highwood, E. J., Turnbull, K., Haywood, J., & Coe, H. (2011). Black carbon aerosol mixing state, organic aerosols and aerosol optical properties over the United Kingdom. *Atmospheric Chemistry and Physics*, 11(17), 9037–9052. <http://doi.org/10.5194/acp-11-9037-2011>
- Momenimovahed, A. & Olfert, J. S. (2015). Effective Density and Volatility of Particles Emitted from Gasoline Direct Injection Vehicles and Implications for Particle Mass Measurement. *Aerosol Science & Technology* 49(11), 1051-1062. <http://doi.org/10.1080/02786826.2015.1094181>
- Moteki, N., & Kondo, Y. (2007). Effects of Mixing State on Black Carbon Measurements by Laser-Induced Incandescence. *Aerosol Science and Technology*, 41(4), 398–417. <http://doi.org/10.1080/02786820701199728>
- Myhre, G., Shindell, D., Breon, F.-M., Collins, W., Fuglestedt, J., Huang, J., ... Zhang, H. (2013). *Anthropogenic and Natural Radiative Forcing*. In T. F. Stocker, D. Qin, G.-K. Plattner, M. Tignor, S. K. Allen, J. Boschung, ... P. M. Midgley (Eds.), *Climate Change 2013: The Physical Science Basis. Contribution of Working Group I to the Fifth Assessment Report of the Intergovernmental Panel on Climate Change*. Cambridge, UK and New York, NY, USA: *Cambridge University Press*. Retrieved from http://www.climatechange2013.org/images/report/WG1AR5_Chapter08_FINAL.pdf
- NIOSH. (2003). Monitoring of Diesel Particulate Exhaust in the Workplace, Chapter Q, Third Supplement to NMAM, in NIOSH Manual of Analytical Methods, 4th ed., P. F. O'Connor, P. C. Schlecht, eds., NIOSH, Cincinnati, OH, USA. NIOSH DHHS Publication No. 2003-154
- Official Journal of the European Union (2012). Commission Regulation (EC) No 459/2012.
- Olfert, J., Collings, N. (2005). New method for particle mass classification – the Couette centrifugal particle mass analyzer. *Journal of Aerosol Science*. 36:1338-1352.
- Onasch, T. B., Trimborn, A., Fortner, E. C., Jayne, J. T., Kok, G. L., Williams, L. R., ... Worsnop, D. R. (2012). Soot Particle Aerosol Mass Spectrometer: Development, Validation, and

- Initial Application. *Aerosol Science and Technology*, 46(7), 804–817.
<http://doi.org/10.1080/02786826.2012.663948>
- Pagels, J., Khalizov, A. F., McMurry, P. H., & Zhang, R. Y. (2009). Processing of Soot by Controlled Sulphuric Acid and Water Condensation—Mass and Mobility Relationship. *Aerosol Science and Technology*, 43(7), 629–640.
<http://doi.org/10.1080/02786820902810685>
- Petzold, A., Ström, J., Ohlsson, S., Schröder, F. P. (1998). Elemental composition and morphology of ice-crystal residual particles in cirrus clouds and contrails. *Atmospheric Research*. 49(1):21-34.
- Petzold, A., Fiebig, M., Fritzsche, L., Stein, C., Schumann, U., Wilson, C. W., ... Technology, C. (2005). Particle emissions from aircraft engines – a survey of the European project PartEmiss. *Meteorologische Zeitschrift*, 14(4), 465–476. <http://doi.org/10.1127/0941-2948/2005/0054>
- Petzold, A., Ogren, J., Fiebig, M., Laj, P., Li, S.-M., Baltensperger, U., ... Zhang, X.-Y. (2013). Recommendations for reporting "black carbon" measurements. *Atmospheric Chemistry and Physics*, 13, 8365-8379. doi:10.5194/acp-13-8365-2013
- Pope, C. A. (2000). What do epidemiologic findings tell us about health effects of environmental aerosols? *Journal of Aerosol Med.* 13(4):335-354.
- Radney, J. G. and Zangmeister, C. D. (2016). Practical limitations of aerosol separation by a tandem differential mobility analyzer-aerosol particle mass analyzer. *Aerosol Science and Technology*. doi: 10.1080/02786826.2015.1136733
- Rawata, V. K., Buckleya, D. T., Kimotoa, S., Leeb M.-H., Fukushima, N., Hogan, C. J. (2016). Two dimensional size–mass distribution function inversion from differential mobility analyzer–aerosol particle mass analyzer (DMA–APM) measurements. *Journal of Aerosol Science* 92, 70-82. doi:10.1016/j.jaerosci.2015.11.001
- Ris, C. (2008). U.S. EPA Health assessment for diesel engine exhaust: A review. research-article. Retrieved 09.05.14, from <http://informahealthcare.com/doi/abs/10.1080/08958370701497960>.
- Rissler, J., Nordin, E., Eriksson, A., Nilsson, P., Frosch, M., Sporre, M., ... Swietlicki, E. (2014). Effective Density and Mixing State of Aerosol Particles in a Near-Traffic Urban Environment. *Environ. Sci. Technol.*, 48 (11), pp 6300–6308. doi: 10.1021/es5000353
- Ristimäki, J., Vaaraslahti, K., Lappi, M., and Keskinen, J. (2007). Hydrocarbon Condensation in Heavy-Duty Diesel Exhaust. *Environ. Sci. Technol.*, 41:6397–6402.
- SAE. (2011). SAE Aerospace Recommended Practice 1179 Rev D, "Aircraft gas turbine engine exhaust smoke measurement". *Society of Automotive Engineers International*.

- SAE. (2013). Aerospace Information Report (AIR) 6241, Procedure for the Continuous Sampling and Measurement of Non-Volatile Particle Emissions from Aircraft Turbine Engines. *SAE International*, Warrendale, PA
- Sakurai, H., Park, K., McMurry, P. H., Zaring, D. D., Kittleson, D. B., and Ziemann, P. J. (2003). Size-Dependent Mixing Characteristics of Volatile and Nonvolatile Components in Diesel Exhaust Aerosols. *Environ. Sci. Technol.*, 37:5487–5495.
- Schnitzler, E., Dutt, A., Charbonneau, A., Olfert, J. S., and Jaeger, W. (2014) Soot aggregate restructuring due to coatings of secondary organic aerosols derived from aromatic precursors. *Environmental Science & Technology*, 48:14309-14316.
- Schwarz, J. P., Spackman, J. R., Gao, R. S., Perring, A. E., Cross, E., Onasch, T. B., Ahern, A., Wrobel, W., Davidovits, P., Olfert J., Dubey, M. K., Mazzoleni C. & Fahey D. W. (2010). The Detection Efficiency of the Single Particle Soot Photometer. *Aerosol Science and Technology*, 44(8), 612-628. <http://doi.org/10.1080/02786826.2010.481298>
- Schindler, W., Haisch, C., Beck, H., Niessner, R., Jacob, E., Rothe, D. (2004). A Photoacoustic Sensor System for Time Resolved Quantification of Diesel Soot Emissions. *SAE Technical Papers*.
- Snelling, D., Smallwood, G., Liu, F., Gülder, Ö., Bachalo, W. (2005). A calibration-independent laser-induced incandescence technique for soot measurement by detecting absolute light intensity. *Applied Optics*. 44:6773-6785.
- Sorensen, C. M. (2011) The Mobility of Fractal Aggregates: A Review. *Aerosol Science & Technology* 45(7), 765-779. doi: 10.1080/02786826.2011.560909
- Stettler, Marc E. J., Swanson, Jacob J., Barrett, Steven R. H., Bois, Adam M. (2013) Updated Correlation Between Aircraft Smoke Number and Black Carbon Concentration. *Aerosol Science and Technology*. 47(11):1205-1214.
- Stephens, M., Turner, N., & Sandberg, J. (2003). Particle Identification by Laser-Induced Incandescence in a Solid-State Laser Cavity. *Applied Optics*, 42(19), 3726. <http://doi.org/10.1364/AO.42.003726>
- Stipe, C., Higgins, B., Lucasa, D., Koshland, C., Sawyer, R. (2005). Inverted Co-Flow Diffusion Flame for Producing Soot. *Review of Scientific Instruments*. 76:23–908.
- Stolzenburg, M. R., & McMurry, P. H. (2008). Equations Governing Single and Tandem DMA Configurations and a New Lognormal Approximation to the Transfer Function. *Aerosol Science and Technology*, 42(6), 421–432. <http://doi.org/10.1080/02786820802157823>
- Swanson, J.J., & Schulz, H.-J. (2013). “Measurement of solid particle concentration is aided by catalytic stripper technology”. Poster presented at *European Aerosol Conference 2013*.
- Symonds, J., Reavell, K., Olfert, J. (2013). The CPMA-Electrometer System – A Suspended Particle Mass Concentration Standard. *Aerosol Science and Technology*. 47(8):i-iv.

- Tajima, N., Fukushima, N., Ehara, K., Sakurai, H. (2011). Mass Range and Optimized Operation of the Aerosol Particle Mass Analyzer. *Aerosol Science and Technology*. 45(2):196-214.
- Unal, A., Hu, Y. T., Chang, M. E., Odman, M. T., and Russell, A. G., "Airport Related Emissions and Impacts on Air Quality: Application to the Atlanta International Airport," *Atmospheric Environment*, Vol. 39, No. 32, 2005, pp. 5787–5798.
doi:10.1016/j.atmosenv.2005.05.051
- UNECE Regulation No. 83 (Emissions of M1 and N1 categories of vehicles). Available at:
<http://www.unece.org/trans/main/wp29/wp29regs81-100.html>
- Wang, S. C., & Flagan, R. C. (1990). Scanning Electrical Mobility Spectrometer. *Aerosol Science and Technology*, 13(2), 230–240. <http://doi.org/10.1080/02786829008959441>
- Wang, Q., Huang, R.-J., Cao, J., Han, Y., Wang, G., Li, G., ... Zhou, Y. (2014). Mixing State of Black Carbon Aerosol in a Heavily Polluted Urban Area of China: Implications for Light Absorption Enhancement. *Aerosol Science and Technology*, 48(7), 689–697.
<http://doi.org/10.1080/02786826.2014.917758>
- Woody, M., Baek, B. H., Adelman, Z., Omary, M., Lam, Y. F., West, J. J., and Arunachalam, S., "An Assessment of Aviation's Contribution to Current and Future Fine Particulate Matter in the United States," *Atmospheric Environment*, Vol. 45, No. 20, 2011, pp. 3424–3433.
doi:10.1016/j.atmosenv.2011.03.041
- Yim, Steve H. L., Stettler, Marc E. J., Barrett, Steven R. H. (2013). Air quality and public health impacts of UK airports. Part II: Impacts and policy assessment. *Atmospheric Environment*. 67:184-192.
- Zhang, R., Khalizov, A. F., Pagels, J., Zhang, D., Xue, H., & McMurry, P. H. (2008). Variability in morphology, hygroscopicity, and optical properties of soot aerosols during atmospheric processing. *Proceedings of the National Academy of Sciences of the United States of America*, 105(30), 10291–6. Retrieved from
<http://www.pnas.org/cgi/content/abstract/105/30/10291>

Appendix A. Supplementary Material to Mixing State of Particles Emitted from a Gas Turbine Engine

A.1 Volatile Number and Mass Fractions with Upstream Catalytic Stripper

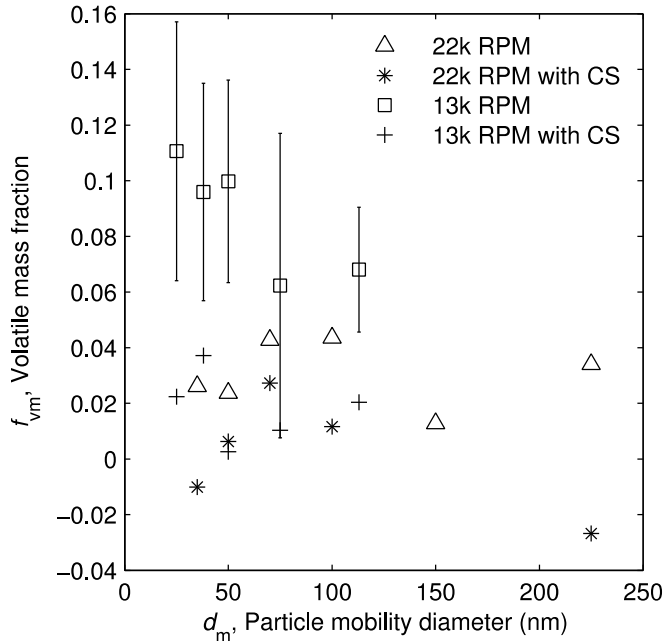


Figure A.1: Volatile mass fraction versus particle mobility diameter for particulate from a Gnome engine at 22,000 RPM and 13,000 RPM, with the upstream catalytic stripper (CS) either off or on. The error bars on the 13,000 RPM data points represent 95% confidence intervals, from approximately 5 measurements per data point.

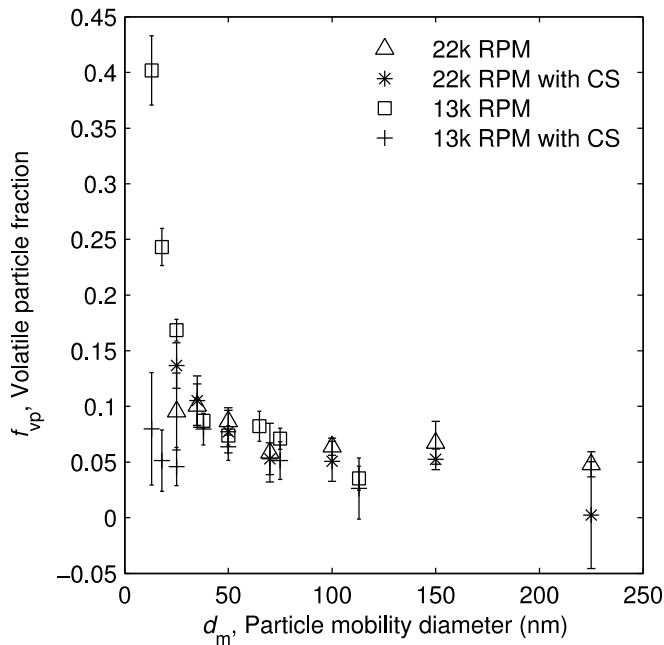


Figure A.2: Volatile particle number fraction versus particle mobility diameter for particulate from a Gnome engine at 22,000 RPM and 13,000 RPM, with the upstream catalytic stripper (CS) either off or on. The error bars on the 13,000 RPM data points represent 95% confidence intervals, from approximately 10 measurements per data point.

Measurements of the volatile mass and number fractions were also taken with the upstream catalytic stripper (CS) turned on, in order to confirm that the catalytic denuder was removing all volatile material. Figure S1 shows the volatile mass fractions with the CS on, compared to the volatility measurements made with it turned off. The volatile mass fractions measured in this case were as high as 4%, but also included obviously unphysical negative values of similar magnitude. The averages of these measurements were approximately 1% for the 13,000 RPM condition and 0% for the 22,000 RPM condition, indicating the volatile mass fraction measurements have an uncertainty on the order of a few percent, and possibly that the removal of volatile material in the upstream CS is incomplete. Figure S2 similarly shows the volatile number fractions with the CS on. These measurements showed volatile number fractions of around 5%, rather than zero. Again, this may indicate that the removal of volatile material in the upstream CS is incomplete. A possible reason for this is that the upstream catalytic stripper was handling a higher flow rate and a higher concentration of particulate matter than the catalytic denuder in the DMA-CPMA system, so it may have been less effective. This discrepancy does not affect the volatility measurements presented in this paper, which did not use the upstream catalytic stripper.